

FACULTY
OF MATHEMATICS
AND PHYSICS
Charles University

MASTER THESIS

Michal Gregor

Tidal heating and heat transfer in the ice shell of Jupiter's moon Europa

Department of Geophysics

Supervisor of the master thesis: prof. RNDr. Ondřej Čadek, CSc.

Study programme: Mathematical and Computational Modeling in Physics

Prague 2025

I declare that I carried out this master thesis on my own, and only with the cited sources, literature and other professional sources. I understand that my work relates to the rights and obligations under the Act No. 121/2000 Sb., the Copyright Act, as amended, in particular the fact that the Charles University has the right to conclude a license agreement on the use of this work as a school work pursuant to Section 60 subsection 1 of the Copyright Act.

In ..... date ....

Author's signature

First, I want to thank my partner Pavlína, who has supported me throughout the writing of this thesis. She gave me emotional support when I felt down and overwhelmed. She also read the thesis, found multiple errors, and gave me helpful suggestions on how to improve the writing. I am also very thankful to my parents and grandfather, who supported me financially by giving me a place to live and food to eat, so I could focus on studying.

But most of all, I am grateful to my supervisor, Prof. Čadek. I want to thank him for reading the early versions of my diploma thesis and giving me many suggestions on how to improve it. I also want to thank him, and perhaps even apologize, because I know I wasn't always the easiest student to work with. I worked on this thesis for about 2.5 years, which is too long. This was mainly because I took on too many additional responsibilities, either by taking extra courses or starting to gain some early work experience. As a result, the work on my diploma thesis suffered. There were even periods when I didn't touch it for several months and almost forgot where I had left off. Eventually, I would pick it back up and continue. I am truly grateful to Prof. Čadek for not giving up on me and for always being willing to help whenever I was ready to continue. I also really appreciated our consultation talks, not only did I receive valuable feedback for my thesis, but we also had interesting discussions about science and the academic system in general. Prof. Čadek might have wanted me to pursue a PhD in geophysics, but he always encouraged me to follow my own interests above all.

Title: Tidal heating and heat transfer in the ice shell of Jupiter's moon Europa

Author: Michal Gregor

Department: Department of Geophysics

Supervisor: prof. RNDr. Ondřej Čadek, CSc., Department of Geophysics

Abstract: This thesis investigates the thermal behavior of Europa's ice shell under tidal deformation. We develop a global model that couples viscoelastic deformation with heat conduction, using Maxwell rheology and temperature-dependent viscosity. Our main focus is on the stationary solution of the model, used to analyze temperature profiles, tidal dissipation, and heat fluxes. We examine how these fields vary with respect to two key parameters: ice shell thickness and basal viscosity. The results show that tidal dissipation can strongly localize near the base of the shell and significantly alter internal temperature distributions and inner boundary heat flux. However, the outer boundary heat flux is largely unaffected by tidal heating and is mainly determined by the imposed boundary condition. We identify critical combinations of parameters that lead to the onset of melting.

Keywords: Europa, tidal heating, viscoelasticity, Maxwell rheology, heat conduction, ice shell

Název práce: Slapové zahřívání a přenos tepla v ledové slupce Jupiterova měsíce Europy

Autor: Michal Gregor

katedra: katedra geofyziky

Vedoucí diplomové práce: prof. RNDr. Ondřej Čadek, CSc., katedra geofyziky

Abstrakt: Tato práce se zabývá tepelným chováním ledové slupky Europy při slapových deformacích. Vyvinuli jsme globální model, který spojuje viskoelastickou deformaci s vedením tepla, přičemž využíváme Maxwellovu reologii a viskozitu závislou na teplotě. Zaměřujeme se především na stacionární řešení rovnic, u kterého zkoumáme teplotní profily, slapovou disipaci a tepelné toky na hranicích. Zkoumáme, jak se tato pole mění s ohledem na dva klíčové parametry: tloušťku ledové slupky a viskozitu na spodním rozhraní voda/led. Výsledky ukazují, že slapová disipace se může silně lokalizovat na spodní hranici slupky a významně měnit rozložení vnitřní teploty a tepelný tok na vnitřní hranici. Tepelný tok na vnější hranici však není slapovým zahříváním do značné míry ovlivněn a je určen především okrajovou podmínkou. Identifikujeme kritické kombinace parametrů, které vedou k tavení slupky.

Klíčová slova: Europa, slapové ohřívání, viskoelasticita, Maxwellova reologie, vedení tepla, ledová slupka

Contents

Introduction **7**

1 About Europa **9**

2 Mathematical Formulation of the Problem **12**
2.1 Governing Equations 12
2.2 Parameters of the Model 16

3 Solution Method **18**
3.1 Deformation and Heat Conduction Timescale Split 18
3.2 The Spherical Harmonic Representation 19
3.2.1 Spherical Harmonic Decomposition 20
3.2.2 Transition Between the Harmonic Series and Values on a Grid 21
3.3 The Right-Hand Side of Maxwell's Rheology 22
3.3.1 Nonlinearity in Spherical Harmonic Expansions: Product of Series 23
3.3.2 The Numerical Approximation of the Integral 24
3.4 Radial Discretisation of the Equations 24
3.5 Equations of Viscoelastic Deformation and Their Discretisation . 27
3.5.1 Spheroidal Equations for Degree $j \geq 2$ 28
3.5.2 Spheroidal Equations for Degree $j = 1$ 31
3.5.3 Toroidal Equations for Degree $j \geq 2$ 32
3.6 Calculation of the Dissipation 34
3.7 The Heat Equation in the Spherical Representation 35

4 Results **38**
4.1 Results for the Fixed Parameter $d = 30\,\mathrm{km}$ 38
4.2 Results for Other Values of Thickness d 40

Discussion and Conclusions **49**

A Appendix **51**
A.1 Comment on Uniqueness of the Stationary Solution 51
A.1.1 Uniqueness of the Stationary Heat Equation with Linear Conductivity 51
A.1.2 Uniqueness of the Stationary Heat Equation with Nonlinear Conductivity 52
A.1.3 Uniqueness in the Case of Temperature-Dependent Heating 54
A.2 Spherical Harmonic Functions 55
A.2.1 Scalar Spherical Harmonic Functions 55
A.2.2 Vector Spherical Harmonic Functions 56
A.2.3 Tensor Spherical Harmonic Functions 57
A.2.4 Clebsch-Gordan Coefficients 59
A.2.5 Wigner 6j-symbols 60
A.2.6 Differential Operators 61

A.2.7 Other Useful Formulas 62

Bibliography **64**

Introduction

Icy moons of the outer Solar System have emerged as some of the most interesting and intensively studied objects in planetary science. Despite their cold surfaces, many of them show signs of geological activity and are believed to harbor global subsurface oceans beneath their outer ice shells. These hidden oceans are among the prime candidates in the search for extraterrestrial life. Instead of solar heating, internal energy sources, especially tidal heating, are believed to maintain these oceans in a liquid state by converting orbital and rotational energy into heat.

Europa, one of Jupiter's largest moons, is a particularly notable example. Observations from space missions have provided strong evidence for a liquid water ocean beneath its icy surface, and surface features suggest ongoing geological activity. The main source of internal energy is Europa's tidal deformation, driven by its slightly eccentric orbit and the strong gravitational pull from Jupiter. These regular deformations generate frictional heat inside the moon's interior, making tidal heating a key process for understanding both Europa's thermal evolution and its potential habitability.

Tidal heating plays a major role not only for Europa, but also for other moons such as Io, Ganymede, and Enceladus, and may also be relevant for certain exoplanets. As such, it remains an active area of research in planetary science. Modeling these effects is crucial for understanding the thermal structure, dynamics, and long-term evolution of icy moons. One key question is whether these subsurface oceans can remain stable over geological timescales. Since life, if it exists, would need millions of years to develop, it is important to assess whether these environments are stable enough to sustain it.

In this thesis, we study the thermal behavior of Europa's ice shell, focusing on heating caused by tidal deformation. We implement and analyze the solutions of a discretized system of partial differential equations describing the viscoelastic deformation of the shell, coupled with an equation governing heat conduction. The ice is modeled as a Maxwell viscoelastic material, with viscosity depending exponentially on temperature. This introduces strong coupling between the mechanical and thermal behavior of the shell.

There have been many modeling efforts aimed at understanding Europa's interior and heat sources. Some focus on the subsurface ocean, others simulate the entire interior as a coupled system, and some target the ice shell using increasingly sophisticated rheological models. Our aim is to contribute to this research by developing a global shell model that captures the interaction between tidal heating and temperature-dependent viscosity.

We aim to answer several key questions: What does the steady-state temperature distribution in the shell look like? How is tidal dissipation distributed, and where is it strongest? How does dissipation influence the heat flux from the ocean into the shell and through the outer surface? How does the total volumetric heat production compare to the energy fluxes at the boundaries? Under what conditions does the ice shell begin to melt?

Because of significant uncertainties in key parameters, particularly the ice shell thickness and the reference viscosity at the ice-ocean interface, we treat these

as free parameters and systematically study how the model responds to their variation. We are especially interested in identifying combinations of parameters that lead to thermal instability or partial melting.

We hope that this simplified yet global approach offers meaningful insights into the physical processes governing Europa's ice shell and clarifies the role of tidal heating in maintaining a potentially habitable subsurface ocean.

1 About Europa

Europa is one of the four large Galilean moons orbiting Jupiter. With a mean radius of approximately 1,560 km, it is slightly smaller than Earth's Moon and ranks as the sixth-largest moon in the Solar System. A global view of Europa is shown in Figure 1.1.

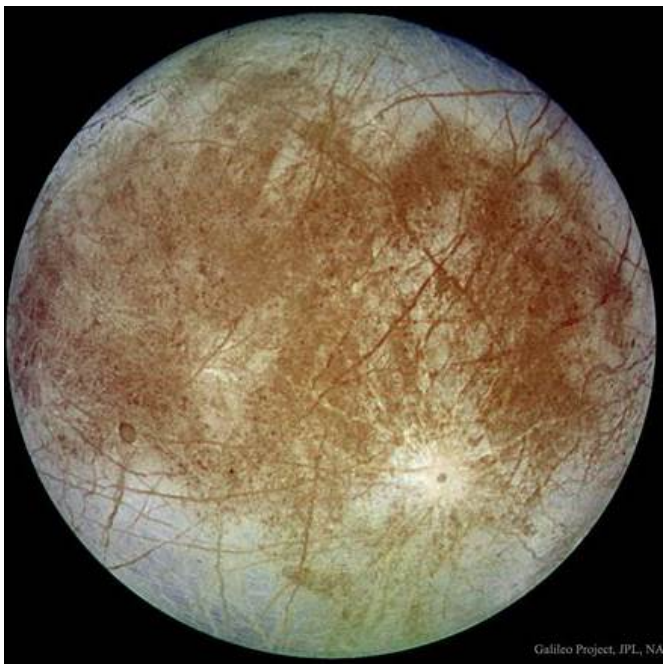


Figure 1.1 Europa as seen by the Galileo spacecraft in 1996. Image credit: NASA/JPL/Galileo Project.

Europa is an icy moon with a geologically young surface, characterized by its bright ice, long dark lineae (stripes), and a surprisingly low number of impact craters. In fact, Europa has the smoothest surface of any known solid body in the Solar System. This smoothness and lack of craters suggest recent surface renewal driven by internal heat [1]. Europa's icy shell exhibits a rich variety of surface morphologies, as illustrated in Figure 1.2, including intersecting ridges, disrupted blocks, and impact structures that hint at an active geological history.

The main source of internal heating is thought to be tidal dissipation. Europa has an orbital period of 3.5 days and an eccentricity ($e \approx 0.009$), which leads to periodic deformation as the moon moves closer to and farther from Jupiter. Because the interior is not perfectly elastic, this flexing generates friction and heat [2]. It is widely believed that beneath the icy shell lies a global subsurface ocean. This is mainly supported by magnetic field measurements from the Galileo spacecraft, which are consistent with an electrically conductive, salty liquid layer under the surface [3]. The combined thickness of the ice and ocean is estimated to be around 100 km. Beneath that lies a rocky mantle and possibly a metallic core. A schematic of the internal structure is shown in Figure 1.3.

Surface temperatures are extremely low, around 100 K at the equator and 50 K at the poles, so the ice is very stiff near the surface. The persistence of a liquid ocean implies that internal heating must be strong enough to prevent

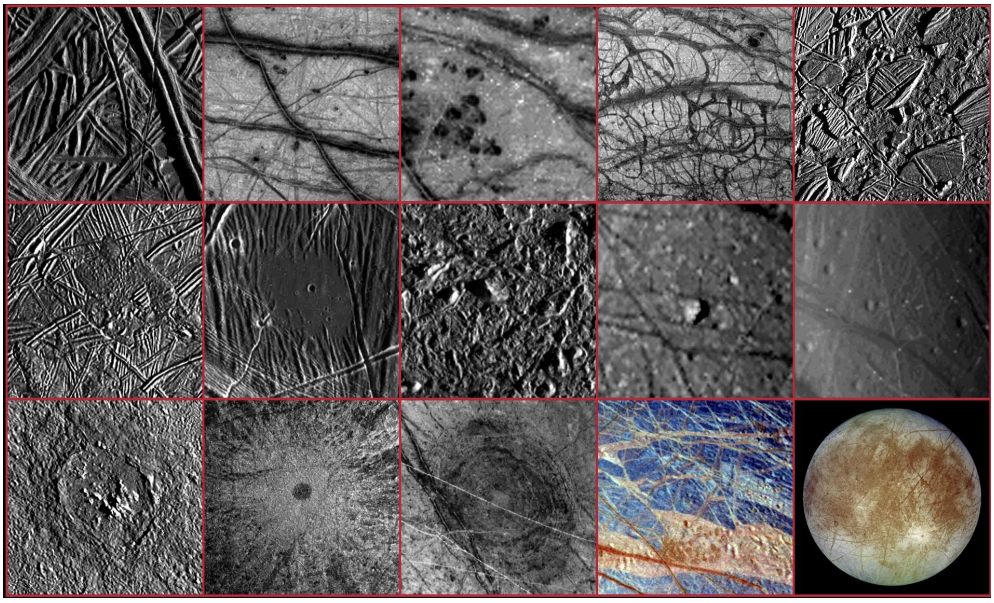


Figure 1.2 Composite image showing examples of various surface features observed on Europa, including ridges, bands, chaotic terrain, and craters. Image credit: NASA/JPL/DLR.

the entire layer from freezing. Europa is also a prime candidate in the search for extraterrestrial life. It is possible that hydrothermal vents on the ocean floor, similar to "black smokers" found on Earth, could provide the heat and nutrients needed to support microbial ecosystems, even without sunlight [4]. There is also growing evidence of plume activity: jets of water vapor erupting from the surface. Observations by the Hubble Space Telescope suggest that these plumes occasionally erupt from the south polar region. Some researchers believe the Galileo spacecraft may have flown through one such plume. An illustration of this phenomenon is shown in Figure 1.4.

Europa's surface also shows a complex network of ridges, bands, and chaotic terrains where blocks of ice appear to have broken and refrozen. These features may indicate local melting and upwelling from the subsurface ocean. Most of our current knowledge comes from NASA's *Galileo* mission (1995–2003). Two major new missions are now underway: NASA's *Europa Clipper*, launched in 2024, will fly by Europa many times to investigate its ocean, surface, and ice shell. ESA's *JUICE* mission (JUpiter ICy moons Explorer), launched in 2023, will also study Europa during several flybys, though its primary target is Ganymede. These missions are expected to improve our understanding of Europa's internal structure and its potential to support life.

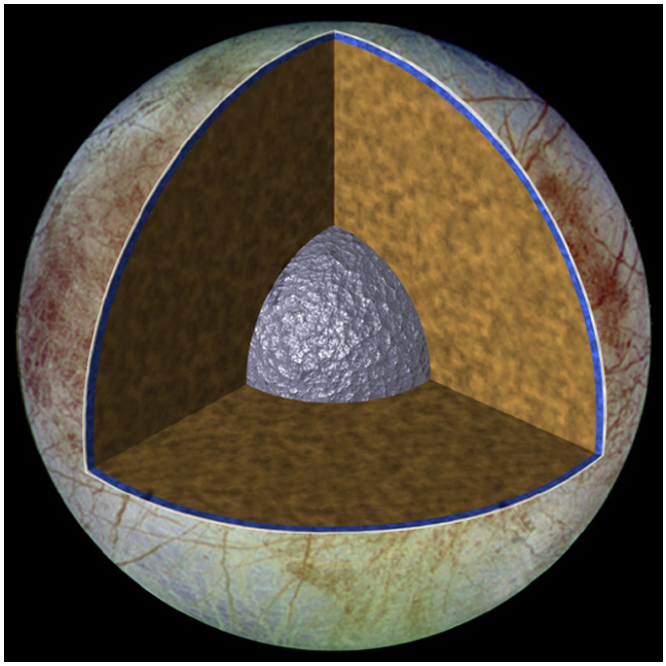


Figure 1.3 Cutaway illustration of Europa's possible internal structure. The model shows a metallic core, a rocky mantle, a liquid water ocean, and an outer ice shell. The surface image is based on data from the Galileo spacecraft; the internal layers are inferred from magnetic and gravity measurements. Image credit: NASA/JPL.

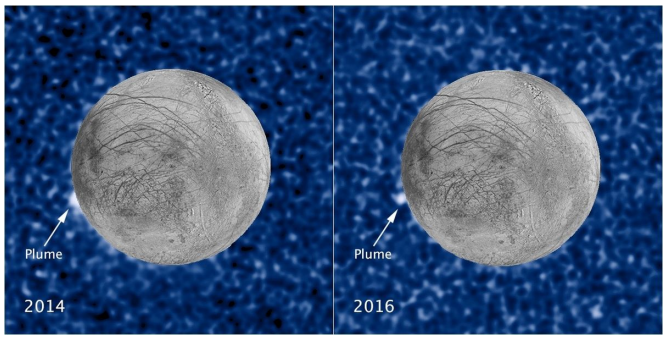


Figure 1.4 Suspected water plume observed erupting from Europa's surface. The composite image combines data from the Hubble Space Telescope and NASA's Galileo spacecraft, showing plume activity detected in the same region at two different times. Image credit: NASA, ESA, and W. Sparks (STScI); illustration credit: NASA, ESA, W. Sparks (STScI), and USGS Astrogeology Science Center.

2 Mathematical Formulation of the Problem

In this chapter, we present our mathematical model of viscoelastic deformation and heat conduction within Europa's ice shell, in the form of partial differential equations. These are very common equations in the continuum mechanics [5, 6], but what makes it nontrivial is the geometry and mainly the nonlinear dependence of viscosity on temperature.

2.1 Governing Equations

Our solution domain Ω is a spherical shell, the region between two spheres of different radii, i.e.,

$$\Omega = \{x \in \mathbb{R}^3;\ R_b \leq \|x\| \leq R_t\},$$

where R_b is the inner radius, i.e., the distance from Europa's center to the base of the ice shell, and R_t is the outer radius. The thickness of the shell is given by $d = R_t - R_b$, as illustrated in Figure 2.1.

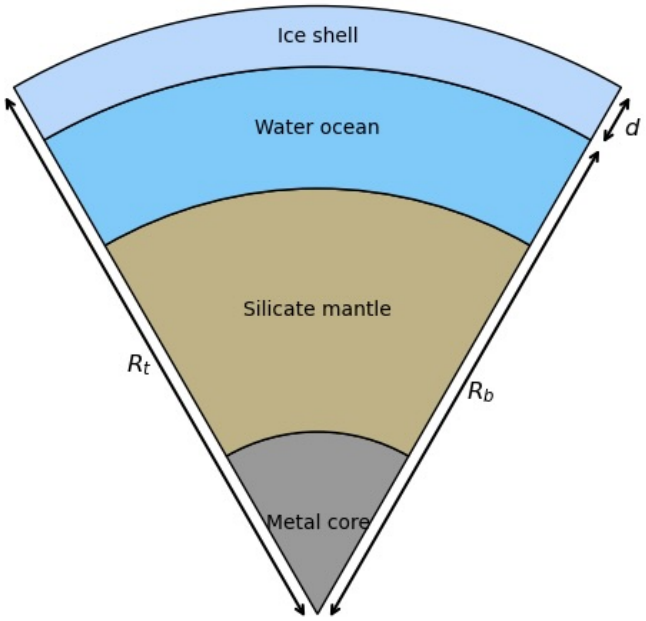


Figure 2.1 Schematic illustration of Europa's internal structure, showing the inner radius R_b, the outer radius R_t, and the shell thickness d.

We are solving evolutionary equations, so our unknown functions are defined on $(0, t_{max}) \times \Omega$, with some maximal time t_{max}. We define the space-time domain as follows:

$$\mathcal{Q} = (0, t_{max}) \times \Omega, \quad \mathcal{Q}_b = (0, t_{max}) \times \partial\Omega_b, \quad \mathcal{Q}_t = (0, t_{max}) \times \partial\Omega_t.$$

Here, we refer to $\partial\Omega_b$ as the bottom boundary of the ice shell, given by $\|x\| = R_b$ and $\partial\Omega_t$ as the top boundary, given by $\|x\| = R_t$.

Our unknown functions are temperature $T = T(t, x)$, the displacement vector $\mathbf{u} = \mathbf{u}(t, x)$, and the Cauchy stress tensor $\boldsymbol{\tau} = \boldsymbol{\tau}(t, x)$, representing deviations from hydrostatic equilibrium, and we want them to be the solution of the following boundary value, initial value problem:

$$
\begin{aligned}
0 &= \nabla \cdot \mathbf{u}(t,x) && \text{in } \mathcal{Q}, && (2.1a)\\
0 &= \nabla \cdot \boldsymbol{\tau}(t,x) - \rho_i \nabla (V_t(t,x) + V_g(t,x)) && \text{in } \mathcal{Q}, && (2.1b)\\
\boldsymbol{\tau}^D(t,x) &= \mu((\nabla \mathbf{u}(t,x)) + (\nabla \mathbf{u}(t,x))^T) - \mu \int_0^t \frac{\boldsymbol{\tau}^D(t',x)dt'}{\eta(T(t',x))} && \text{in } \mathcal{Q}, && (2.1c)\\
\boldsymbol{\tau}(t,x) \cdot \mathbf{e}_r &= -\rho_i g_t u_r(t,x)\mathbf{e}_r, && \text{at } \mathcal{Q}_t, && (2.1d)\\
-\boldsymbol{\tau}(t,x) \cdot \mathbf{e}_r &= -\Delta\rho g_b u_r(t,x)\mathbf{e}_r - \rho_w (V_t(t,x) + V_g(t,x))\mathbf{e}_r && \text{at } \mathcal{Q}_b, && (2.1e)\\
\rho_i c_p \dot{T}(t,x) &= \nabla \cdot (k(T(t,x))\nabla T(t,x)) + h(t,x) && \text{in } \mathcal{Q}, && (2.1f)\\
T(t,x) &= T_t(x) && \text{at } \mathcal{Q}_t, && (2.1g)\\
T(t,x) &= T_b(x) && \text{at } \mathcal{Q}_b, && (2.1h)\\
T(0,x) &= T_0(x) && \text{in } \Omega, && (2.1i)
\end{aligned}
$$

where μ is the shear modulus of ice, ρ_i the density of ice, g_b and g_t the gravitational accelerations at the bottom and top of the shell, c_p the thermal capacity of ice at constant pressure, ρ_w the density of water, and $\Delta\rho = \rho_w - \rho_i$ are all constants. All other symbols appearing in the system of equations (2.1) will be explained in this section. The viscosity η is a function of temperature, generally expressed in the form of an exponential function:

$$\eta(t,x) = \eta_0 \exp\left(\frac{E}{RT_b}\left(\frac{T_b}{T(t,x)} - 1\right)\right), \tag{2.2}$$

where η_0 is the reference viscosity at the ice-ocean boundary, where the temperature is equal to $T_b = 273\,\mathrm{K}$, the melting temperature of ice, $E = 59\,\mathrm{kJ\,mol^{-1}}$ is the activation energy for diffusion creep, and $R = 8.314\,\mathrm{J\,mol^{-1}\,K^{-1}}$ is the universal gas constant [7, 8].

The thermal conductivity $k(t, x)$ is given by a nonlinear temperature dependence:

$$k(t,x) = \frac{k_0}{T(t,x)}, \tag{2.3}$$

where k_0 is a constant [9] and the source term $h(t, x)$ is given by a formula [10]:

$$h(t,x) = \frac{\boldsymbol{\tau}^D(t,x) : \boldsymbol{\tau}^D(t,x)}{2\eta(T(t,x))}. \tag{2.4}$$

The first three equations of (2.1), together with the boundary conditions (2.1d) and (2.1e), are the classical linearized equations of viscoelastic deformation in continuum mechanics. The first equation (2.1a), which states that the divergence of the displacement field is zero, expresses our assumption that the material is incompressible and that we are dealing with small deformations. The second equation (2.1b) represents the balance of momentum (Newton's second law), with the left-hand side, which contains accelerations, neglected. This approximation is commonly used in geophysical simulations, where accelerations in solid materials

within planetary bodies are often negligible. The term $V_t(t,x)$ on the right-hand side represents the tidal potential, given in spherical coordinates (r,θ,ϕ) by

$$\begin{aligned} V(t,r,\theta,\phi) = r^2\omega^2 e\Bigg[&\sqrt{\frac{9\pi}{5}}\cos(\omega t)Y_{20}(\theta,\phi) - \\ &- \left(\sqrt{\frac{27\pi}{10}}\cos(\omega t) - i\sqrt{\frac{24\pi}{5}}\sin(\omega t)\right)Y_{22}(\theta,\phi) - \\ &- \left(\sqrt{\frac{27\pi}{10}}\cos(\omega t) + i\sqrt{\frac{24\pi}{5}}\sin(\omega t)\right)Y_{2-2}(\theta,\phi)\Bigg], \end{aligned} \tag{2.5}$$

where ω is the angular frequency of Europa's periodic motion around Jupiter, e is the eccentricity of its elliptical orbit, and $Y_{jm}(\theta,\phi)$ are spherical harmonic functions of degree j and order m. More details on their definition and properties are provided in the appendix section A.2.1. It is notable that the tidal potential has such a simple analytical expression in terms of spherical harmonics, involving only degree $j=2$ and orders $m=-2,0,2$ [11]. The second potential term $V_g(t,x)$ is the self-gravity potential describing the change in the gravitational field caused by the deformation of the body. For our spherical shell case, it takes the relatively simple form [12]:

$$\begin{aligned} V(t,r,\theta,\phi) = \sum_{j=1}^{j_{\max}}\sum_{m=0}^{j}\Bigg[&-\frac{4\pi G r}{2j+1}\left(\frac{R_b}{r}\right)^{j+2}\Delta\rho\,(u_r)_{jm}(t,R_b) - \\ &- \frac{4\pi G r}{2j+1}\left(\frac{r}{R_t}\right)^{j}\rho_i\,(u_r)_{jm}(t,R_t)\Bigg]Y_{jm}(\theta,\phi), \end{aligned} \tag{2.6}$$

where G is the gravitational constant and $(u_r)_{jm}$ are the spherical harmonic coefficients of the radial displacement at the top and bottom boundaries of the shell. The summation runs to degree $j_{\max}$, which corresponds to the maximum degree of our spherical harmonic approximation (more on this later in 3.2).

The third equation (2.1c) is the rheological relation describing the material's response to stress, linking the Cauchy stress tensor $\boldsymbol{\tau}(t,x)$ with the displacement vector $\mathbf{u}(t,x)$. This corresponds to the Maxwell rheology of viscoelastic deformation, characterized by two parameters: the shear modulus μ (assumed constant) and the viscosity η, which strongly depends on temperature. Maxwell rheology is formally a model for a viscoelastic fluid, but it is widely used in geophysics and planetary science to model solid materials, such as ice in our case. The reason for this is that it remains relatively simple to implement while being empirically powerful and descriptive [5].

Equation (2.1c) is not necessarily the most general form of Maxwell's rheology. A more rigorous and objective (frame-invariant) formulation is the Upper Convected Maxwell model, originally proposed by Oldroyd [13], written in terms of the velocity field $\mathbf{v}$ as

$$\frac{\mu}{\eta}\boldsymbol{\tau} + \left(\frac{\partial\boldsymbol{\tau}}{\partial t} + \mathbf{v}\cdot\nabla\boldsymbol{\tau} - \mathbf{L}\cdot\boldsymbol{\tau} - \boldsymbol{\tau}\cdot\mathbf{L}^T\right) = 2\mu\mathbf{D}, \tag{2.7}$$

where $\mathbf{L}$ is the velocity gradient tensor, and $\mathbf{D}$ is its symmetric part:

$$\mathbf{D} = \frac{1}{2}(\mathbf{L}+\mathbf{L}^T). \tag{2.8}$$

The entire bracketed expression in (2.7) represents the Oldroyd derivative. To derive equation (2.1c), we neglect all nonlinear terms in the Oldroyd derivative, keeping only the partial time derivative, since we are dealing with small deformations. Integrating the equation from 0 to t transforms the symmetric velocity gradient into the symmetric displacement gradient, and gives rise to the integral term on the right-hand side of (2.1c).

The deformation equations are supplemented with the boundary conditions (2.1d) and (2.1e), which describe a free surface with dynamic topography. The terms $\boldsymbol{\tau}(t,x)\cdot\mathbf{e}_r$ at the upper boundary and $-\boldsymbol{\tau}(t,x)\cdot\mathbf{e}_r$ at the lower boundary are the tracktion vectors, as defined by the Cauchy stress tensor. The vector $\mathbf{e}_r$ is the unit radial vector, directed outward from the center. Consequently, $\mathbf{e}_r$ serves as the outward normal vector at the upper boundary, while $-\mathbf{e}_r$ is the outward normal vector at the lower boundary. The term $u_r(t,x)$ denotes the radial displacement at the boundary. Further, we introduce the term $\rho_w(V_t(t,x)+V_g(t,x))$ in the bottom boundary condition to account for pressure from the subsurface ocean. This follows from the equilibrium condition between pressure and body forces:

$$0 = -\nabla p - \rho_w \nabla(V_t + V_g), \tag{2.9}$$

which implies

$$p = \text{Const} - \rho_w(V_t + V_g). \tag{2.10}$$

Since we solve the system in a spherical harmonic representation for degree $j \geq 1$, we can ignore the constant term, which would appear only for $j = 0$. This will be clarified further in Section 3.2.

Equation (2.1f) represents the heat equation, which describes heat conduction within the material. It is a standard parabolic equation governing the evolution of the temperature field with a temperature dependent conductivity. The source term given by (2.4) arises from internal friction due to viscoelastic deformation and thus serves as a coupling term between the deformation and heat equation.

The heat equation is subject to the Dirichlet boundary conditions (2.1g) and (2.1h), which are time-independent. The lower boundary condition is straightforward: a constant temperature of 273K (the melting point of ice), corresponding to the ice-ocean interface. The upper boundary condition is a prescribed temperature distribution that depends only on the meridional angle θ and is symmetric with respect to the equator. This profile reflects the variation in solar insolation, with higher temperatures near the equator and lower temperatures near the poles. It reaches a maximum of approximately 95K at the equator and a minimum of about 50K at the poles [14]. The function is shown in Figure (2.2). The initial temperature distribution $T_0(x)$ must also be specified.

These are the equations that we aim to solve, our mathematical model of the physical phenomenon. The system consists of two interconnected parts: the first is the set of equations describing viscoelastic deformation, including the balance of momentum, Maxwell's rheology, the incompressibility condition, and boundary conditions. The second part is the heat equation with Dirichlet boundary conditions, which governs the conduction of heat within the material and describes the time evolution of temperature. These two parts are coupled through the heat source term $h(t,x)$ in the heat equation, which arises from the dissipation of viscoelastic deformation. This means that the mechanical deformation generates heat, which influences the temperature distribution. Conversely, the temperature

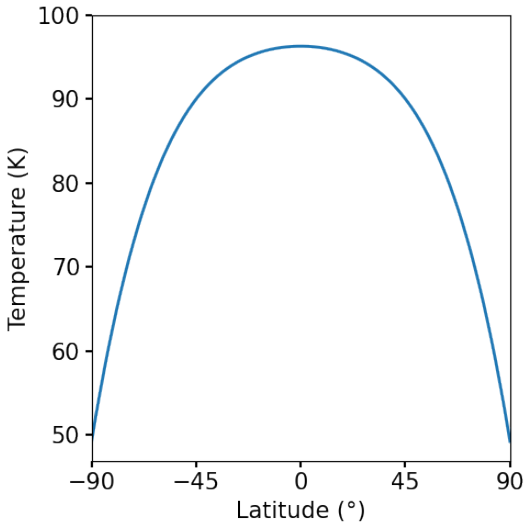


Figure 2.2 Temperature field at the outer boundary, showing a maximum of approximately 95 K at the equator and a minimum of about 50 K at the poles (from [14]).

field affects the deformation equations via the viscosity η in the Maxwell rheology, which depends strongly on temperature. Thus, the viscosity, determined by the temperature field, influences the mechanical response of the material, while the dissipation from deformation serves as a heat source, affecting the thermal evolution. Together, these two interdependent processes form a complex nonlinear system that describes the thermal evolution of the ice shell of Europa.

2.2 Parameters of the Model

In this section, we list all the parameters and physical constants used in our mathematical model. As seen in the previous chapter, the model incorporates various parameters, so it is beneficial to clearly present them all in one place.

Parameter	**Symbol**	**Value**	**Units**
Inner radius of Europa	R_{bot}	1531	km
Shear modulus of ice	μ	3.3×10^{15}	Pa
Gravity at the top of the ice shell	g_{top}	1.314	m/s^2
Gravity at the bottom of the ice shell	g_{bot}	1.314	m/s^2
Ice density	ρ_{ice}	920	kg/m^3
Water density	ρ_{water}	1000	kg/m^3
Angular frequency	ω	2.04783×10^{-5}	s^{-1}
Orbital eccentricity	e	0.009	-
Thermal conductivity constant	k_0	651	W/m
Isobaric heat capacity of ice	c_p	2108	J/kg K

Table 2.1 Fixed physical parameters used in the model.

The reference viscosity η_0, which appears in the temperature-dependent viscosity law (see Equation (2.2)), is treated as a free model parameter and is varied to study how the results depend on the rheological properties of the ice. Lower values of η_0 correspond to weaker, more dissipative ice, while very high values

approach the elastic limit, where almost no dissipation occurs. The considered range $(5 \times 10^{13}, 1 \times 10^{16})$ Pa·s reflects physically realistic estimates, with lower values corresponding to very small ice grain sizes [7] and upper values approaching nearly elastic behavior. Similarly, the ice shell thickness d is also varied, since its value is uncertain and may range from about 10 km to 70 km. We consider the interval $(10, 50)$ km in our simulations. This variation allows us to assess how the results and thermal stability of the shell depend on geometry.

3 Solution Method

In this chapter, we present in detail the methods used to solve the equations introduced and motivated in the previous chapter. First, we explain why we do not simulate the system as a whole but instead split it into deformation and heat conduction parts due to the fundamental difference in their characteristic timescales. Next, we introduce spherical harmonic expansions, i.e., we approximate all functions as finite spherical harmonic series. Following that, we dedicate a section to the nonlinearity in spherical expansions, particularly the product of series. Subsequently, we present the deformation equations in their spherical representation and describe how they are radially discretised. A similar section follows for the heat equation, where the spherical representation is comparatively simpler.

3.1 Deformation and Heat Conduction Timescale Split

The system of equations (2.1) consists of two interconnected parts: deformation and heat conduction. Deformation influences heat conduction through the dissipative heat source, while heat conduction, in turn, affects deformation through the viscosity's dependence on temperature. When numerically simulating the time evolution of any system, we must discretise continuous time t using a time step Δt, which is typically chosen as a fraction, such as 1%, of some characteristic timescale of the system.

The issue here is that the characteristic timescale of the deformation equations is dramatically shorter than that of the heat conduction equation. The characteristic timescale for deformation is given by

$$\tau_d = \min\{T_p, \frac{\eta}{\mu}\}, \tag{3.1}$$

where $T_p = 3.551$ days is the orbital period of Europa around Jupiter, and the second term, the ratio of viscosity to shear modulus, corresponds to the characteristic timescale of Maxwell's model, the so called Maxwell time. This means that the timescale of deformation is on the order of a few days, requiring a discretisation time step of at most a few hours.

By non-dimensionalizing the heat equation (2.1f) using a characteristic time scale τ, a characteristic temperature $\overline{T}$, and a characteristic length scale given by the shell thickness d, we obtain the expression

$$\tau = \frac{\rho_i c_p d^2 \overline{T}}{k_0}. \tag{3.2}$$

Substituting the parameter values from Table (2.1), with $\overline{T} = 200$ K and shell thickness in the range $d = 10$–70 km, yields a characteristic timescale τ in the interval approximately 2×10^6–9.5×10^7 years.

This enormous difference in timescales is a key challenge in simulating the system. While the characteristic time for deformation is only a few days, the heat

conduction timescale is millions of years. If we were to simulate the entire system with a single shared time step, we would have to choose the smaller one dictated by the deformation equations. This would mean updating heat dissipation and viscosity at every deformation time step, but because the temperature evolves extremely slowly, we would need an enormous number of time steps to observe any significant temperature change.

To address this issue, we use an approach commonly applied in such cases: splitting the system into two separate parts, deformation and heat conduction, and evolving them separately in an alternating way, always evolving only one part while keeping the results from the other constant. The simulation starts with an initial temperature distribution, from which we compute the viscosity field. The deformation equations are then solved for several orbital periods while keeping the viscosity constant and computing the dissipation as the average over one period,

$$\overline{h}(x) = \frac{1}{T_p} \int_0^{T_p} h(t', x) dt'. \tag{3.3}$$

Once the deformation reaches a converged state, the heat equation is evolved with its much larger time step to allow for a meaningful temperature change. The viscosity field is then updated based on the new temperature, and the process repeats. This way, we effectively simulate the evolution of the coupled system.

There are two expected scenarios for the system. Either the system will converge to a stationary state, where the temperature and dissipation fields stop changing over time, or it will diverge. In the second case, the dissipation becomes very high in some areas, which causes the temperature to rise, and that makes the dissipation even higher, until the system 'blows up', this is called thermal runaway. In that case, the temperature goes over 273K, the melting point of ice, which our equations don't take into account, so the result becomes physically meaningless. We initially tried to model the melting scenario too by limiting the temperature at 273K and introducing a simple melting rule, but it turned out to be quite complicated and we didn't make much progress with it. We note that the evolutionary problem (2.1) is somewhat artificial, since we are not really interested in how the system evolves from its initial condition, which is rather arbitrary, but rather in the stationary solution it converges to. We devote a short section in appendix A.1, where we comment on the uniqueness of the stationary solution.

3.2 The Spherical Harmonic Representation

When numerically solving differential equations, we always have to choose some finite-dimensional approximation of the functions. A natural idea would be to use the Finite Element Method (FEM). The equations (2.1) are quite straightforward and should be relatively easy to implement using a package like FEniCS, for example. The problem with the finite element method in this case is the geometry and the required resolution. Europa is quite large, with a radius of 1531 km, but the ice shell is only approximately 10-50 km thick. Since we need a fine resolution within the ice shell, covering the whole domain with a sufficiently fine mesh would require an enormous number of elements. For this reason, we decided to use the

spectral method, meaning that we approximate our solution functions by a finite series of spherical harmonic functions.

3.2.1 Spherical Harmonic Decomposition

We expand all the functions we are solving for in a spherical harmonic series: as a superposition of scalar spherical harmonic functions (which form an orthonormal basis of L^2 functions on a sphere), vector spherical harmonic functions (an orthonormal basis of L^2 vectors on a sphere), and tensor spherical harmonic functions (an orthonormal basis of L^2 tensors on a sphere), as follows:

$$T(t,r,\theta,\phi) = \sum_{j=0}^{j_{\max}} \sum_{m=-j}^{j} T_{jm}(t,r) Y_{jm}(\theta,\phi), \tag{3.4a}$$

$$\mathbf{u}(t,r,\theta,\phi) = \sum_{j=0}^{j_{\max}} \sum_{m=-j}^{j} \sum_{l=|j-1|}^{j+1} u^l_{jm}(t,r) \mathbf{Y}^l_{jm}(\theta,\phi), \tag{3.4b}$$

$$\boldsymbol{\tau}(t,r,\theta,\phi) = \sum_{j=0}^{j_{\max}} \sum_{m=-j}^{j} \tau^{j0}_{jm}(t,r) \mathbf{Y}^{j0}_{jm}(\theta,\phi) + \sum_{j=0}^{j_{\max}} \sum_{m=-j}^{j} \sum_{l=|j-2|}^{j+2} \tau^{l2}_{jm}(t,r) \mathbf{Y}^{l2}_{jm}(\theta,\phi), \tag{3.4c}$$

where $\mathbf{Y}^l_{jm}(\theta,\phi)$ are the vector spherical harmonic functions and $\mathbf{Y}^{l2}_{jm}(\theta,\phi)$ are the tensor spherical harmonic functions. A detailed definition and the properties of spherical harmonic functions can be found in the appendix A.2. This means that all the dependence on the spherical angles θ and ϕ is contained in the basis functions, and we only solve for the coefficients of the linear combinations, which are functions of time t and radial distance r. The first term in the Cauchy stress expansion corresponds to the isotropic (pressure) part, while the second term represents the deviatoric (traceless) part of the stress tensor.

The sums go from degree $j = 0$ to $j = j_{\max}$, so this is a finite-dimensional approximation. The parameter $j_{\max}$ is an important parameter of the numerical simulation, as it determines the lateral resolution. The higher the $j_{\max}$, the better the resolution on the sphere, but of course, increasing $j_{\max}$ also increases the computational cost.

The spherical harmonic series also has an important property (A.10): if the expanded function is real, then the coefficient of order $-m$ is the complex conjugate of the coefficient of order $+m$, multiplied by $(-1)^m$. This allows us to solve only for the coefficients with order $m \geq 0$.

The idea of the spectral method is now to substitute these spherical harmonic decompositions into the equations in (2.1), use analytical formulas for differential operators (A.57) acting on the product of a radially dependent function and a harmonic function, and expand the result again in terms of spherical harmonics. Thanks to the orthogonality of the harmonics, when we multiply the equation by a basis function and integrate over the sphere, the Kronecker delta appears and selects only the coefficient corresponding to the given basis function. This causes the equations to separate for different degrees and orders, so instead of solving a system of partial differential equations, we get a system of ordinary differential equations for each degree and order, with only radial and time derivatives.

The beauty of the spectral method is most evident in the linear setting. Unfortunately, this is not exactly our case, since the integral on the right-hand

side of Maxwell's rheology contains the product of the Cauchy stress and the inverse of viscosity, both of which we want to expand in a harmonic series. More about this will be discussed in the next chapter.

The spectral method is also particularly useful when the driving force has a simple representation in the basis functions. This is exactly the case for the tidal force described by the tidal potential (2.5), which has only a few nontrivial coefficients at degree $j = 2$ and orders $m = -2, 0, 2$. If the equations were linear and if the viscosity depended only on the radial coordinate, then we would only need to solve the deformation equations for this specific degree and these two orders. All the other coefficients would trivially be zero.

The spectral method also seems convenient in the case when the basis functions somehow respect the symmetry of the problem, that is why the spherical harmonic functions are so often used in geophysics and planetary science, because they respect the spherical symmetry, which can be often found in planetary bodies. The degree $j = 0$ corresponds to the spherically symmetrical case, where all the quantities depend only on the radial distance, and all the higher terms can be seen as somewhat a correction of the spherically symmetrical case.

3.2.2 Transition Between the Harmonic Series and Values on a Grid

We often need to perform operations on functions expanded in spherical harmonic series. Linear operations, for example, are straightforward. If we have two functions f and g with harmonic series representations

$$f(\theta,\phi) = \sum_{j=0}^{j_{\max}} \sum_{m=-j}^{j} f_{jm} Y_{jm}(\theta,\phi), \quad g(\theta,\phi) = \sum_{j=0}^{j_{\max}} \sum_{m=-j}^{j} g_{jm} Y_{jm}(\theta,\phi),$$

then, of course, it follows that

$$\begin{aligned}(af + bg)(\theta,\phi) &= a \sum_{j=0}^{j_{\max}} \sum_{m=-j}^{j} f_{jm} Y_{jm}(\theta,\phi) + b \sum_{j=0}^{j_{\max}} \sum_{m=-j}^{j} g_{jm} Y_{jm}(\theta,\phi) \\ &= \sum_{j=0}^{j_{\max}} \sum_{m=-j}^{j} (a f_{jm} + b g_{jm}) Y_{jm}(\theta,\phi).\end{aligned}$$

However, things become much more complicated when performing nonlinear transformations, such as computing the logarithm of a function:

$$\ln(f(\theta,\phi)) = \ln\left(\sum_{j=0}^{j_{\max}} \sum_{m=-j}^{j} f_{jm} Y_{jm}(\theta,\phi) \right),$$

where we would still like to keep the function in the spherical harmonic representation:

$$\ln(f(\theta,\phi)) = \sum_{j=0}^{j_{\max}} \sum_{m=-j}^{j} (\ln f)_{jm} Y_{jm}(\theta,\phi).$$

In such cases, we proceed by evaluating the function on a discrete grid on the sphere. For example, we use a 360×180 grid, with 360 equally spaced points for a given constant θ, and 180 equally spaced points for a given constant ϕ. From these

discrete values, we compute the spherical harmonic coefficients by numerically approximating the integrals (A.8).

For these operations, we use highly efficient Fortran programs: HARMSY (harmonic synthesis, which converts harmonic coefficients to grid values) and HARMAN together with HARMLS (harmonic analysis, which converts grid values back to harmonic coefficients). These programs were developed at the Department of Geophysics. The process is illustrated in Figure 3.1.

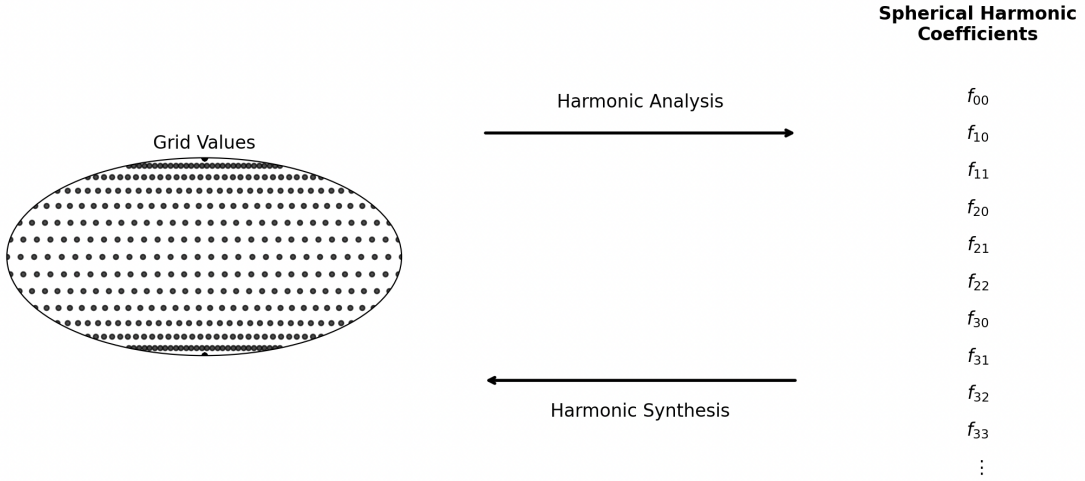


Figure 3.1 Transition between grid values and spherical harmonic coefficients.

3.3 The Right-Hand Side of Maxwell's Rheology

As mentioned earlier, the beauty of the spectral method shines the most in linear cases, where the equations perfectly separate into different degrees and orders without the need to handle products of harmonic series. This is even more apparent when the driving force has a simple expression in the corresponding basis, such as a finite superposition of a few terms, like the tidal force. In that case, we can solve the system only for these specific degrees and orders.

What complicates the problem are nonlinearities, which break this simplicity and force us to solve the system across all degrees and orders. However, nonlinear problems are ubiquitous in nature and are of great interest. Our system (2.1) contains three nonlinearities. The first one appears in the heat equation (2.1f), where the conductivity k is a function of temperature, i.e., $k = k(T)$. This particular nonlinearity can be handled effectively using a trick, thanks to the specific nature of its dependence (more details are given in the heat equation section 3.7). The second nonlinearity is found in the dissipation term (2.4), where the viscosity in the denominator depends exponentially on temperature. This is manageable, and we describe the method used to compute dissipation in a dedicated section 3.6.

The third nonlinearity is more challenging: the integral on the right-hand side of Maxwell's rheology involving the deviatoric part of the Cauchy stress tensor multiplied by the inverse viscosity, which depends on temperature. Both of these quantities are expressed as harmonic series.

3.3.1 Nonlinearity in Spherical Harmonic Expansions: Product of Series

We need to deal with the term

$$\int_0^t \frac{\boldsymbol{\tau}^D(t',x)dt'}{\eta(T(t',x))}, \tag{3.5}$$

where the deviatoric part of the Cauchy stress tensor is expanded as a harmonic series:

$$\boldsymbol{\tau}^D(t,r,\theta,\phi) = \sum_{j=0}^{j_{\max}} \sum_{m=-j}^{j} \sum_{l=|j-2|}^{j+2} \tau_{jm}^{l2}(t,r) Y_{jm}^{l2}(\theta,\phi).$$

Let us denote the inverse of viscosity as ξ and refer to it as fluidity:

$$\xi(t,x) = \frac{1}{\eta(T(t,x))}. \tag{3.6}$$

Since viscosity depends on temperature, which varies laterally, we also express fluidity in a spherical harmonic expansion:

$$\xi(t,r,\theta,\phi) = \sum_{j=0}^{j_{\max}} \sum_{m=-j}^{j} \xi_{jm}(t,r) Y_{jm}(\theta,\phi). \tag{3.7}$$

Thus, we are dealing with a product of two series:

$$\begin{aligned} &\boldsymbol{\tau}^D(t,r,\theta,\phi)\xi(t,r,\theta,\phi) = \\ &= \left(\sum_{j=0}^{j_{\max}} \sum_{m=-j}^{j} \sum_{l=|j-2|}^{j+2} \tau_{jm}^{l2}(t,r) Y_{jm}^{l2}(\theta,\phi) \right) \left(\sum_{j=0}^{j_{\max}} \sum_{m=-j}^{j} \xi_{jm}(t,r) Y_{jm}(\theta,\phi) \right), \end{aligned} \tag{3.8}$$

which we want to express again as a harmonic series for a deviatoric tensor:

$$(\boldsymbol{\tau}^D\xi)(t,r,\theta,\phi) = \sum_{j=0}^{j_{\max}} \sum_{m=-j}^{j} \sum_{l=|j-2|}^{j+2} (\boldsymbol{\tau}^D\xi)_{jm}^{l2}(t,r) Y_{jm}^{l2}(\theta,\phi). \tag{3.9}$$

The main challenge in computing the product of two spherical harmonic series comes from the fact that their multiplication increases the maximum degree of the resulting series. This is evident from the formula for the product of two spherical harmonics [15]:

$$Y_{j_1m_1}Y_{j_2m_2} = \sum_{j=|j_1-j_2|}^{j_1+j_2} \sum_{m=-j}^{j} \sqrt{\frac{(2j_1+1)(2j_2+1)}{4\pi(2j+1)}} C_{j_1m_1j_2m_2}^{jm} C_{j_10j_20}^{j0} Y_{jm}, \tag{3.10}$$

where $C_{j_1m_1j_2m_2}^{jm}$ are Clebsch-Gordon coefficients. These coefficients, which are discussed in more detail in the appendix A.2.4, frequently appear in spherical harmonic manipulations. A key implication of this formula is that the product of two harmonics of degree up to $j_{\max}$ produces terms with degrees up to $2j_{\max}$. In our implementation, however, we retain only coefficients up to $j_{\max}$, assuming that the higher-order contributions are small and can be neglected.

Obtaining the product coefficients $(\boldsymbol{\tau}^D\xi)_{jm}^{l2}$ from the original τ_{jm}^{l2} and ξ_{jm} is therefore not straightforward. While analytical expressions exist, they are quite

involved and impractical for implementation. Instead, we use a code developed by Prof. Martinec that computes the product numerically. The method involves evaluating the fields on a grid, applying a Fast Fourier Transform in the azimuthal direction, and other tricks. We only had to modify the original code to make it compatible with a modern Fortran.

3.3.2 The Numerical Approximation of the Integral

Here, we describe how we numerically approximate the integral in (3.5), given that we are working with discrete timesteps instead of continuous time. We approximate it in a straightforward way:

$$\int_0^t \frac{\boldsymbol{\tau}^D(t', x)dt'}{\eta(T(t', x))} \approx \sum_{i=0}^{N-1} \frac{\boldsymbol{\tau}^D(i\Delta t, x)\Delta t}{\eta(T(i\Delta t, x))}, \tag{3.11}$$

where $N\Delta t = t$, starting from $\boldsymbol{\tau}^D(0, x) = 0$. This causes a small disturbance at the beginning, but it converges quickly. This is perhaps the simplest way to approximate the integral using step functions, as illustrated in Figure (3.2).

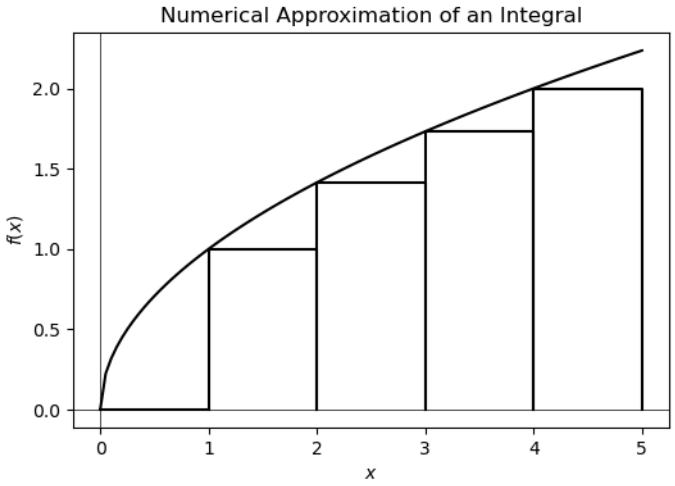


Figure 3.2 Illustration of the numerical approximation of the integral using step functions. The integral is approximated as a sum of discrete rectangular areas, representing the left Riemann sum.

The implementation is straightforward. We store the cumulative integral in memory and update it at each step by adding the product of the deviatoric part of the Cauchy stress tensor and the fluidity from the previous step, multiplied by the timestep.

3.4 Radial Discretisation of the Equations

When substituting the spherical harmonic expansions of functions into the equations in system of equations (2.1), we obtain differential equations for the harmonic coefficients, which are functions of only time and the radial distance. Specifically, we get an ordinary differential equation in the radial variable for the

coefficients in the deformation equations at a given time and a partial differential equation in time and radial distance for the coefficients in the heat equation.

We have already discussed the discretisation in time, where calculations are performed at discrete time steps. However, an additional discretisation is required in the radial direction. We discretise the radial interval $[R_{\text{bot}}, R_{\text{bot}} + d]$ using a grid of N equidistant points r_i, such that $r_1 = R_{\text{bot}}$ and $r_N = R_{\text{bot}} + d$, as illustrated in Figure 3.3. With this approach, the radial discretisation step, the distance

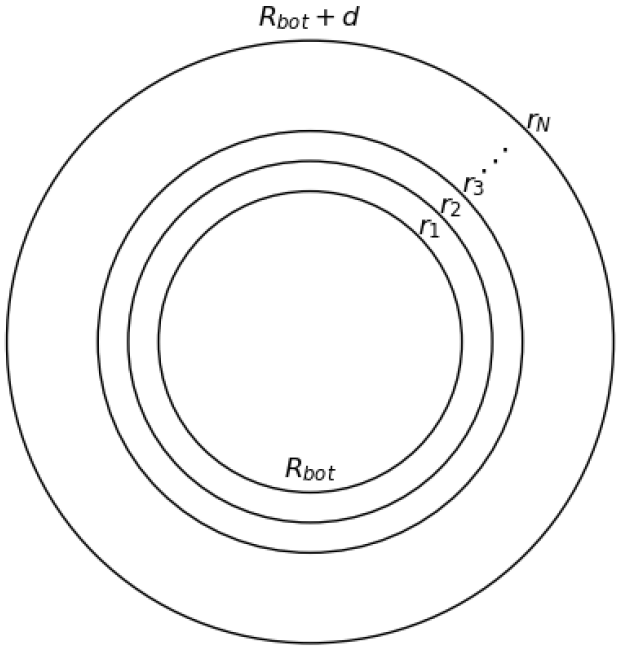


Figure 3.3 Radial discretisation of the domain. The radial interval $[R_{\text{bot}}, R_{\text{bot}} + d]$ is discretized into N equidistant points r_i, where $r_1 = R_{\text{bot}}$ and $r_N = R_{\text{bot}} + d$.

between two consecutive layers, is given by:

$$\Delta r = \frac{d}{N-1}.$$

Some of our functions, such as the deviatoric part of the Cauchy stress tensor $\boldsymbol{\tau}^D(t, r, \theta, \phi)$, dissipation $h(t, r, \theta, \phi)$, and fluidity $\xi(t, r, \theta, \phi)$, are defined at discrete time steps and on discrete radial layers:

$$\boldsymbol{\tau}^D(t_n, r_i, \theta, \phi), \quad h(t_n, r_i, \theta, \phi), \quad \xi(t_n, r_i, \theta, \phi).$$

However, temperature $T(t, r, \theta, \phi)$, displacement $\vec{u}(t, r, \theta, \phi)$ and body force $\mathbf{f}(t, r, \theta, \phi) = \nabla V_t(t, r, \theta, \phi)$ are instead defined at the midpoints between layers:

$$T(t_n, r_{i+\frac{1}{2}}, \theta, \phi), \quad \mathbf{u}(t_n, r_{i+\frac{1}{2}}, \theta, \phi), \quad \mathbf{f}(t_n, r_{i+\frac{1}{2}}, \theta, \phi),$$

as illustrated in Figure 3.4. The reason for this choice is that in (2.1b), the derivative of the Cauchy stress tensor represents the force, so when approximating the derivative using finite differences, it makes the most sense to define it at the midpoints of the layers. For displacement, rheological equations imply that the derivative of displacement corresponds to the Cauchy stress tensor (2.1c).

Similarly, in the heat equation, we want the heat flux, which is defined by the derivative of temperature, to be well defined at the boundaries. Hence, we work with temperature values at the mid-layers.

To handle boundary values, we also define the displacement and temperature at a half-layer below the bottom boundary and a half-layer above the top boundary, allowing us to approximate boundary values as the average of adjacent layers. The lateral dependence is then represented by the harmonic series at a given layer, meaning that each function at a given time step is expanded in a harmonic series up to degree $j_{\max}$, evaluated at N radial layers (or $N+1$ layers for displacement and temperature). According to (A.11), this results in: $N \times \frac{(j_{\max}+1)(j_{\max}+2)}{2}$ coefficients for a scalar function, $N \times \left(3\left(\frac{j_{\max}(j_{\max}+1)}{2} + j_{\max}\right) + 1\right)$ coefficients for a vector function (A.21), and $N \times \left(5\left(\frac{j_{\max}(j_{\max}+1)}{2} + j_{\max}\right) - 3\right)$ coefficients for a tensor function (A.31). We approximate the radial derivatives in the differential

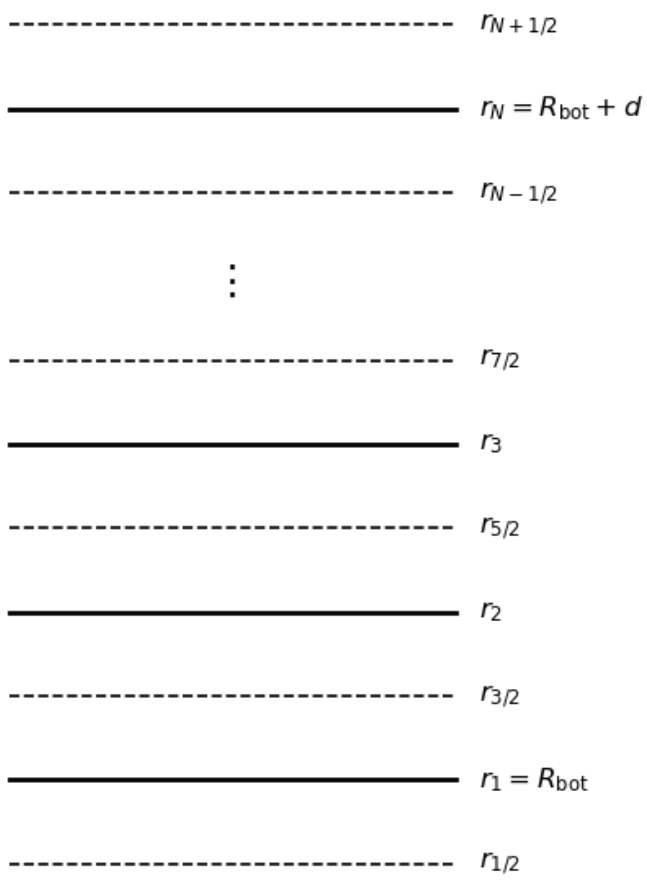


Figure 3.4 Illustration of the radial layer discretisation. The solid lines represent the discrete layers r_i, while the dashed lines indicate the mid-layers $r_{i+\frac{1}{2}}$. The temperature T, displacement $\mathbf{u}$ and body force $\mathbf{f}$ are defined at mid-layers, while deviatoric stress $\boldsymbol{\tau}^D$, dissipation h, and fluidity ξ are defined at the main layers.

equations using finite differences, following the Finite Difference Method:

$$\frac{df(r_{i+\frac{1}{2}})}{dr} \approx \frac{f(r_{i+1}) - f(r_i)}{\Delta r}, \tag{3.12}$$

where the derivative is defined at the midpoint between layers r_i and r_{i+1}.

In the case of the heat equation, where the time derivative of a temperature coefficient depends on its radial first and second derivatives, we approximate the first derivative at a given mid-layer by:

$$\frac{df(r_{i+\frac{1}{2}})}{dr} \approx \frac{f(r_{i+\frac{3}{2}}) - f(r_{i-\frac{1}{2}})}{2\Delta r}, \tag{3.13}$$

and the second derivative by:

$$\frac{d^2 f(r_{i+\frac{1}{2}})}{dr^2} \approx \frac{f(r_{i+\frac{3}{2}}) - 2f(r_{i+\frac{1}{2}}) + f(r_{i-\frac{1}{2}})}{(\Delta r)^2}. \tag{3.14}$$

This arrangement of variables, where some fields are defined at main layers and others at mid-layers, is known as the staggered grid finite difference method. It is a widely used technique in numerical modelling of physical systems, especially those involving fluxes and gradients (e.g., heat conduction, fluid flow, elasticity). The staggered grid improves the numerical stability and accuracy of derivative approximations and helps ensure that fluxes are computed at locations where they are physically meaningful. For smooth functions, the method provides second-order accuracy in space.

3.5 Equations of Viscoelastic Deformation and Their Discretisation

We will not derive these equations in detail here, as the process is quite lengthy. However, the underlying idea is straightforward: we substitute the spherical harmonic expansions into the equations and apply known formulas for how differential operators act on products of scalar radial functions and spherical harmonics. These formulas are listed in Appendix (A.57). This approach yields a system of ordinary differential equations in the radial variable r for the spherical coefficients. Approximating the derivatives by finite differences then leads to a system of linear equations for the coefficients on different layers, which are described by band matrices.

The variables and equations can be categorized into two distinct groups: spheroidal and toroidal. The vector spheroidal coefficients are u_{jm}^{j-1}, u_{jm}^{j+1}, and the tensor spheroidal coefficients are τ_{jm}^{j0}, $\tau_{jm}^{(j-2)2}$, τ_{jm}^{j2}, $\tau_{jm}^{(j+2)2}$. The toroidal coefficients include a single vector coefficient, u_{jm}^{j}, and two tensor coefficients, $\tau_{jm}^{(j-1)2}$ and $\tau_{jm}^{(j+1)2}$.

This distinction has a physical interpretation: spheroidal components describe compressional or extensional deformation, involving both radial and horizontal displacement, and are associated with changes in volume. In contrast, toroidal motion corresponds to purely horizontal, volume-preserving shear deformation, with no radial component. The tidal force is purely spheroidal; thus, if viscosity depended only on radius, we would not need to solve the toroidal equations. However, due to nonlinearity, the harmonic decomposition of the right-hand side of the rheology equations affects all degrees and orders, leading to nontrivial toroidal deformation and motion. Consequently, at each deformation time step, we must solve both spheroidal and toroidal systems for all degrees from $j = 2$

to $j_{\max}$ and for all corresponding orders. Additionally, we solve the spheroidal system for $j = 1$, which is a degenerate case with one fewer tensor coefficient.

3.5.1 Spheroidal Equations for Degree $j \geq 2$

This subsection focuses on the spheroidal equations for degrees $j \geq 2$. After applying the steps outlined in the previous section, we obtain the continuity equation in the form:

$$a_j^1 \frac{du_{jm}^{j-1}(r)}{dr} + a_j^2 \frac{u_{jm}^{j-1}(r)}{r} + b_j^1 \frac{du_{jm}^{j+1}(r)}{dr} + b_j^2 \frac{u_{jm}^{j+1}(r)}{r} = 0, \tag{3.15}$$

the equation of motion:

$$\begin{aligned} &c_j^1 \frac{d\tau_{jm}^{j0}(r)}{dr} + c_j^2 \frac{\tau_{jm}^{j0}(r)}{r} + d_j^1 \frac{d\tau_{jm}^{(j-2)2}(r)}{dr} + d_j^2 \frac{\tau_{jm}^{(j-2)2}(r)}{r} \\ &+ e_j^1 \frac{d\tau_{jm}^{j2}(r)}{dr} + e_j^2 \frac{\tau_{jm}^{j2}(r)}{r} + f_{jm}^{j-1}(r) = 0, \end{aligned} \tag{3.16}$$

$$\begin{aligned} &f_j^1 \frac{d\tau_{jm}^{j0}(r)}{dr} + f_j^2 \frac{\tau_{jm}^{j0}(r)}{r} + g_j^1 \frac{d\tau_{jm}^{j2}(r)}{dr} + g_j^2 \frac{\tau_{jm}^{j2}(r)}{r} \\ &+ h_j^1 \frac{d\tau_{jm}^{(j+2)2}(r)}{dr} + h_j^2 \frac{\tau_{jm}^{(j+2)2}(r)}{r} + f_{jm}^{j+1}(r) = 0, \end{aligned} \tag{3.17}$$

and the rheology equations:

$$\frac{\tau_{jm}^{(j-2)2}(r)}{2\mu} + p_j^1 \frac{du_{jm}^{j-1}(r)}{dr} + p_j^2 \frac{u_{jm}^{j-1}(r)}{r} = -\frac{S_{jm}^{(j-2)2}(r)}{2}, \tag{3.18}$$

$$\frac{\tau_{jm}^{j2}(r)}{2\mu} + q_j^1 \frac{du_{jm}^{j-1}(r)}{dr} + q_j^2 \frac{u_{jm}^{j-1}(r)}{r} + r_j^1 \frac{du_{jm}^{j+1}(r)}{dr} + r_j^2 \frac{u_{jm}^{j+1}(r)}{r} = -\frac{S_{jm}^{j2}(r)}{2}, \tag{3.19}$$

$$\frac{\tau_{jm}^{(j+2)2}(r)}{2\mu} + s_j^1 \frac{du_{jm}^{j+1}(r)}{dr} + s_j^2 \frac{u_{jm}^{j+1}(r)}{r} = -\frac{S_{jm}^{(j+2)2}(r)}{2}, \tag{3.20}$$

where we denoted by S_{jm}^{l2} the coefficients of the right-hand side tensor in the Maxwell rheology equation. This tensor represents the time integral of the product of the deviatoric Cauchy stress with the fluidity. The constant scalar coefficients appearing in the above linear relations are listed in Table 3.1.

Further, we present the discretised form of these equations. We no longer write the indices j, m, as they remain the same for all coefficients. Additionally, we avoid explicitly writing the radial dependence in parentheses and instead use a lower index i to indicate the layer where the given coefficient is defined. To simplify the notation, we denote vector coefficients with $j+1$ and $j-1$ as $+$ and $-$, respectively. Similarly, for tensor coefficients, we use 0, ± 2, and 2 in place of $j0$, $(j \pm 2)2$, and $j2$. The discretised continuity equation is given by:

$$\begin{aligned} &\left(\frac{a_2}{2r_i} - \frac{a_1}{\Delta r}\right) u_{i-\frac{1}{2}}^- + \left(\frac{b_2}{2r_i} - \frac{b_1}{\Delta r}\right) u_{i-\frac{1}{2}}^+ \\ &+ \left(\frac{a_2}{2r_i} + \frac{a_1}{\Delta r}\right) u_{i+\frac{1}{2}}^- + \left(\frac{b_2}{2r_i} + \frac{b_1}{\Delta r}\right) u_{i+\frac{1}{2}}^+ = 0. \end{aligned} \tag{3.21}$$

Coefficient	Expression	Coefficient	Expression
a_j^1	$\sqrt{\frac{j}{2j+1}}$	a_j^2	$-(j-1)a_j^1$
b_j^1	$-\sqrt{\frac{j+1}{2j+1}}$	b_j^2	$(j+2)b_j^1$
c_j^1	$-\sqrt{\frac{j}{3(2j+1)}}$	c_j^2	$(j+1)c_j^1$
d_j^1	$\sqrt{\frac{j-1}{2j-1}}$	d_j^2	$-(j-2)d_j^1$
e_j^1	$-\sqrt{\frac{(j+1)(2j+3)}{6(2j-1)(2j+1)}}$	e_j^2	$(j+1)e_j^1$
f_j^1	$\sqrt{\frac{j+1}{3(2j+1)}}$	f_j^2	$-jf_j^1$
g_j^1	$\sqrt{\frac{j(2j-1)}{6(2j+1)(2j+3)}}$	g_j^2	$-jg_j^1$
h_j^1	$-\sqrt{\frac{j+2}{2j+3}}$	h_j^2	$(j+3)h_j^1$
p_j^1	$-\sqrt{\frac{j-1}{2j-1}}$	p_j^2	jp_j^1
q_j^1	$\sqrt{\frac{(j+1)(2j+3)}{6(2j+1)(2j-1)}}$	q_j^2	$-(j-1)q_j^1$
r_j^1	$-\sqrt{\frac{j(2j-1)}{6(2j+1)(2j+3)}}$	r_j^2	$(j+2)r_j^1$
s_j^1	$\sqrt{\frac{j+2}{2j+3}}$	s_j^2	$-(j+1)s_j^1$

Table 3.1 Coefficients used in the spheroidal equations of deformation, in continuity equation, momentum balance, and rheology equations.

The discretised equations of motion take the form:

$$\begin{aligned}
&\left(\frac{c_2}{2r_{i+\frac{1}{2}}}-\frac{c_1}{\Delta r}\right)\tau_i^0+\left(\frac{d_2}{2r_{i+\frac{1}{2}}}-\frac{d_1}{\Delta r}\right)\tau_i^{-2}+\left(\frac{e_2}{2r_{i+\frac{1}{2}}}-\frac{e_1}{\Delta r}\right)\tau_i^{+2}\\
&+\left(\frac{c_2}{2r_{i+\frac{1}{2}}}+\frac{c_1}{\Delta r}\right)\tau_{i+1}^0+\left(\frac{d_2}{2r_{i+\frac{1}{2}}}+\frac{d_1}{\Delta r}\right)\tau_{i+1}^{-2}\\
&+\left(\frac{e_2}{2r_{i+\frac{1}{2}}}+\frac{e_1}{\Delta r}\right)\tau_{i+1}^{+2}+f_{i+\frac{1}{2}}^-=0, \qquad (3.22)\\
&\left(\frac{f_2}{2r_{i+\frac{1}{2}}}-\frac{f_1}{\Delta r}\right)\tau_i^0+\left(\frac{g_2}{2r_{i+\frac{1}{2}}}-\frac{g_1}{\Delta r}\right)\tau_i^{-2}+\left(\frac{h_2}{2r_{i+\frac{1}{2}}}-\frac{h_1}{\Delta r}\right)\tau_i^{+2}\\
&+\left(\frac{f_2}{2r_{i+\frac{1}{2}}}+\frac{f_1}{\Delta r}\right)\tau_{i+1}^0+\left(\frac{g_2}{2r_{i+\frac{1}{2}}}+\frac{g_1}{\Delta r}\right)\tau_{i+1}^{-2}\\
&+\left(\frac{h_2}{2r_{i+\frac{1}{2}}}+\frac{h_1}{\Delta r}\right)\tau_{i+1}^{+2}+f_{i+\frac{1}{2}}^+=0. \qquad (3.23)
\end{aligned}$$

The discretised rheology equations are given by:

$$\frac{\tau_i^{-2}}{2\mu} + \left(\frac{p_2}{2r_i} - \frac{p_1}{\Delta r}\right) u^-_{i-\frac{1}{2}} + \left(\frac{p_2}{2r_i} + \frac{p_1}{\Delta r}\right) u^-_{i+\frac{1}{2}} = -\frac{S_i^{-2}}{2}, \tag{3.24}$$

$$\frac{\tau_i^{+2}}{2\mu} + \left(\frac{s_2}{2r_i} - \frac{s_1}{\Delta r}\right) u^+_{i-\frac{1}{2}} + \left(\frac{s_2}{2r_i} + \frac{s_1}{\Delta r}\right) u^+_{i+\frac{1}{2}} = -\frac{S_i^{+2}}{2}, \tag{3.25}$$

$$\begin{aligned}\frac{\tau_i^{2}}{2\mu} + \left(\frac{q_2}{2r_i} - \frac{q_1}{\Delta r}\right) u^-_{i-\frac{1}{2}} + \left(\frac{r_2}{2r_i} - \frac{r_1}{\Delta r}\right) u^+_{i-\frac{1}{2}} \\ + \left(\frac{q_2}{2r_i} + \frac{q_1}{\Delta r}\right) u^-_{i+\frac{1}{2}} + \left(\frac{r_2}{2r_i} + \frac{r_1}{\Delta r}\right) u^+_{i+\frac{1}{2}} = -\frac{S_i^{2}}{2}.\end{aligned} \tag{3.26}$$

In total, we have two displacement coefficients defined at $N+1$ mid-layers and four tensor coefficients defined at N layers, resulting in $6N+2$ variables. The continuity equation is defined at layers, contributing N equations, while rheology equations at layers contribute $3N$ equations. The motion equations, defined at the mid-layers, contribute $2(N-1)$ equations. Together, this accounts for $6N-2$ equations, leaving four additional equations required for boundary conditions.

The boundary equations are obtained by applying the formula for the scalar product of spherical functions with the radial unit vector $\mathbf{e}_r$ (A.58). The upper boundary condition is:

$$\begin{aligned}-\sqrt{\frac{j}{3(2j+1)}}\tau^{j0}_{jm} - \sqrt{\frac{(j+1)(2j+3)}{6(2j+1)(2j-1)}}\tau^{j2}_{jm} + \sqrt{\frac{j-1}{2j-1}}\tau^{(j-2)2}_{jm} \\ = -\frac{\rho_w g_t}{2j+1}\left[j u^{j-1}_{jm} - \sqrt{j(j+1)}u^{j+1}_{jm}\right],\end{aligned} \tag{3.27}$$

$$\begin{aligned}\sqrt{\frac{j+1}{3(2j+1)}}\tau^{j0}_{jm} + \sqrt{\frac{j(2j-1)}{6(2j+1)(2j+3)}}\tau^{j2}_{jm} - \sqrt{\frac{j+2}{2j+3}}\tau^{(j+2)2}_{jm} \\ = \frac{\rho_w g_t}{2j+1}\left[\sqrt{j(j+1)}u^{j+1}_{jm} - (j+1)u^{j-1}_{jm}\right].\end{aligned} \tag{3.28}$$

The boundary condition at the lower boundary takes almost the same form as the upper boundary condition, except that the coefficients on the left-hand side have opposite signs due to the reversed direction of the outer boundary. Additionally, instead of ρ_w and g_t, the density difference $\Delta\rho$ and g_b appear, along with an added pressure term. The pressure force can be expressed as

$$\mathbf{p}(\theta,\phi) = -\rho_w\Big(V_t(t,R_b,\theta,\phi) + V_g(t,R_b,\theta,\phi)\Big)\mathbf{e}_r, \tag{3.29}$$

where we use the formula for the product of a scalar spherical harmonic with the radial unit vector $\mathbf{e}_r$, expressed in terms of vector spherical harmonics (A.58). All these equations together form a system of linear equations, represented by a $(6N+2)^2$ band matrix with a bandwidth of 7, as illustrated in Figure 3.5.

The solution vector takes the form

$$(u^-_{\frac{1}{2}}, u^+_{\frac{1}{2}}, \tau^0_1, \tau^{-2}_1, \tau^2_1, \tau^{+2}_1, u^-_{\frac{3}{2}}, u^+_{\frac{3}{2}}, \tau^0_2, \tau^{-2}_2, \tau^2_2, \tau^{+2}_2, ..., \tau^0_N, \tau^{-2}_N, \tau^2_N, \tau^{+2}_N, u^-_{N+\frac{1}{2}}, u^+_{N+\frac{1}{2}}).$$

If we denote by p^l_{jm} the coefficients of the lower boundary pressure force, then the right-hand side takes the form

$$(0, -p^-, -p^+, -\frac{S_1^{-2}}{2}, -\frac{S_1^{2}}{2}, -\frac{S_1^{+2}}{2}, 0, -f^-_{1+\frac{1}{2}}, -f^+_{1+\frac{1}{2}}, -\frac{S_2^{-2}}{2}, -\frac{S_2^{2}}{2}, -\frac{S_2^{+2}}{2}, ...).$$

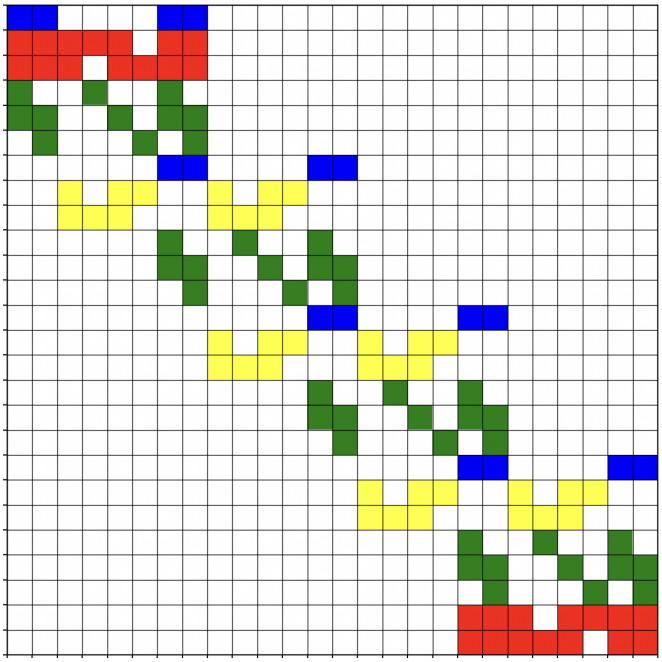


Figure 3.5 Structure of the band matrix of size $(6N+2)^2$ for $N = 4$ with a bandwidth of 7. The different colours correspond to different types of equations: continuity equations (blue), rheology equations (green), boundary conditions (red), and equations of motion (yellow).

The contribution from the tidal force, the main driving force, to the pressure coefficients p^l_{jm} and the volumetric force coefficients f^l_{jm} is nonzero only for degree $j = 2$. For all other degrees, the force arises purely from self-gravitation. All coefficients in Table 3.1 are independent of m, which means that the matrix of the linear system is also independent of m. This allows us to construct the matrix only once for each degree j, and then solve the system for all orders m using different right-hand sides.

Since the harmonic coefficients are generally complex numbers, we solve the system separately for their real and imaginary parts.

3.5.2 Spheroidal Equations for Degree $j = 1$

The case $j = 1$ is a special degenerate one, because the spherical harmonic coefficient $\tau^{(j-2)2}_{jm}$ is not defined for $j = 1$, as the corresponding index $j - 2$ would be negative. In addition, some of the scalar coefficients in the system (listed in Table 3.1) evaluate to zero when $j = 1$. As a result, one of the rheology equations becomes trivially satisfied, since all its terms vanish. Apart from that, the spheroidal equations from the previous section still apply, and the total number of equations is reduced by N compared to the general case.

If the numerical solver were robust enough, it might even be possible to use the same code for solving higher degrees for the case $j = 1$, provided it can handle the additional zeros. However, just to be safe, we treat the case $j = 1$ separately. The resulting $(5N + 2)^2$ band matrix is illustrated in Figure 3.6. The solution vector is in the form

$$(u^-_{\frac{1}{2}}, u^+_{\frac{1}{2}}, \tau^0_1, \tau^2_1, \tau^{+2}_1, u^-_{\frac{3}{2}}, u^+_{\frac{3}{2}}, \tau^0_2, \tau^2_2, \tau^{+2}_2, ..., \tau^0_N, \tau^2_N, \tau^{+2}_N, u^-_{N+\frac{1}{2}}, u^+_{N+\frac{1}{2}}).$$

The right-hand side is

$$(0, -p^-, -p^+, -\frac{S_1^2}{2}, -\frac{S_1^{+2}}{2}, 0, -f^-_{1+\frac{1}{2}}, -f^+_{1+\frac{1}{2}}, -\frac{S_2^2}{2}, -\frac{S_2^{+2}}{2}, ...).$$

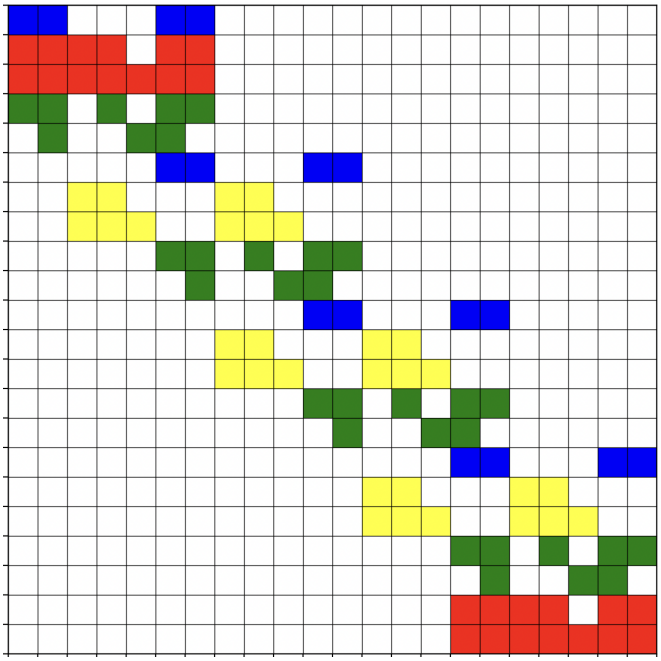


Figure 3.6 Structure of the band matrix of size $(5N+2)^2$ for degree $j = 1$ with $N = 4$ and a bandwidth of 6. The different colours correspond to different types of equations: continuity equations (blue), rheology equations (green), boundary conditions (red), and equations of motion (yellow).

3.5.3 Toroidal Equations for Degree $j \geq 2$

As mentioned above, the tidal force is purely spheroidal. However, due to the nonlinearity of Maxwell's viscoelastic rheology, nontrivial coefficients generally appear in the harmonic series of the deviatoric tensor on the right-hand side of Maxwell's rheology. This results in nonzero toroidal deformation and displacement. The toroidal equations are much simpler. There is only one toroidal vector coefficient, u^j_{jm}, and two tensor coefficients, $\tau^{(j-1)2}_{jm}$ and $\tau^{(j+1)2}_{jm}$. There is no equation of continuity, as toroidal motion automatically maintains volume. The system consists of only one equation of motion and two rheological equations.

The equation of motion takes the form

$$\alpha^1_j \frac{d\tau^{(j-1)2}_{jm}(r)}{dr} + \alpha^2_j \frac{\tau^{(j-1)2}_{jm}(r)}{r} + \beta^1_j \frac{d\tau^{(j+1)2}_{jm}(r)}{dr} + \beta^2_j \frac{\tau^{(j+1)2}_{jm}(r)}{r} = 0, \tag{3.30}$$

and the rheological equations take the form

$$\frac{\tau^{(j-1)2}_{jm}(r)}{2\mu} + \gamma^1_j \frac{du^j_{jm}(r)}{dr} + \gamma^2_j \frac{u^j_{jm}(r)}{r} = -\frac{S^{(j-1)2}_{jm}(r)}{2}, \tag{3.31}$$

$$\frac{\tau^{(j+1)2}_{jm}(r)}{2\mu} + \delta^1_j \frac{du^j_{jm}(r)}{dr} + \delta^2_j \frac{u^j_{jm}(r)}{r} = -\frac{S^{(j+1)2}_{jm}(r)}{2}, \tag{3.32}$$

Coefficient	Expression	Coefficient	Expression
α_j^1	$\sqrt{\frac{j-1}{2j+1}}$	α_j^2	$-(j-1)\alpha_j^1$
β_j^1	$-\sqrt{\frac{j+2}{2(2j+1)}}$	β_j^2	$(j+2)\beta_j^1$
γ_j^1	$-\sqrt{\frac{j-1}{2(2j+1)}}$	γ_j^2	$(j+1)\gamma_j^1$
δ_j^1	$\sqrt{\frac{j+2}{2(2j+1)}}$	δ_j^2	$-j\delta_j^1$

Table 3.2 Coefficients used in the toroidal deformation equations in momentum balance and rheology equations.

where the coefficients are given in Table 3.2.

By approximating the derivatives, we obtain the discretised equation of motion in the form

$$\left(\frac{\alpha_2}{2r_{i+\frac{1}{2}}}-\frac{\alpha_1}{\Delta r}\right)\tau_i^{-1}+\left(\frac{\beta_2}{2r_{i+\frac{1}{2}}}-\frac{\beta_1}{\Delta r}\right)\tau_i^{+1} + \left(\frac{\alpha_2}{2r_{i+\frac{1}{2}}}+\frac{\alpha_1}{\Delta r}\right)\tau_{i+1}^{-1}+\left(\frac{\beta_2}{2r_{i+\frac{1}{2}}}+\frac{\beta_1}{\Delta r}\right)\tau_{i+1}^{+1}+f_{i+\frac{1}{2}}=0, \tag{3.33}$$

and the discretised rheological equations can be written as

$$\frac{\tau_i^{-1}}{2\mu}+\left(\frac{\gamma_2}{2r_i}-\frac{\gamma_1}{\Delta r}\right)u_{i-\frac{1}{2}}+\left(\frac{\gamma_2}{2r_i}+\frac{\gamma_1}{\Delta r}\right)u_{i+\frac{1}{2}}=-\frac{S_i^{-1}}{2}, \tag{3.34}$$

$$\frac{\tau_i^{+1}}{2\mu}+\left(\frac{\delta_2}{2r_i}-\frac{\delta_1}{\Delta r}\right)u_{i-\frac{1}{2}}+\left(\frac{\delta_2}{2r_i}+\frac{\delta_1}{\Delta r}\right)u_{i+\frac{1}{2}}=-\frac{S_i^{+1}}{2}, \tag{3.35}$$

where we simplified the notation for the vector coefficients $u_{jm}^j(r_{i+\frac{1}{2}})$ as $u_{i+\frac{1}{2}}$, and the tensor coefficients $\tau_{jm}^{(j-1)2}(r_i)$ and $\tau_{jm}^{(j+1)2}(r_i)$ as τ_i^{-1} and τ_i^{+1}.

Now, we have $N+1$ displacement coefficients and $2N$ Cauchy stress tensor coefficients, leading to a total of $3N+1$ variables. The system consists of $2N$ rheological equations and $N-1$ equations of motion, since they are defined at the midpoints of layers. The final two necessary equations are the boundary conditions, which take exactly the same form at both the upper and lower boundaries:

$$\sqrt{\frac{j-1}{2(2j+1)}}\tau_{jm}^{(j-1)2}-\sqrt{\frac{j+2}{2(2j+1)}}\tau_{jm}^{(j+1)2}=0. \tag{3.36}$$

All these equations again form a system of linear equations, described by a band matrix of dimensions $(3N+1)^2$ with a bandwidth of 2. The structure of the band matrix is depicted in Figure 3.7.

The solution vector for the toroidal case takes the form

$$(u_{\frac{1}{2}},\tau_1^{-1},\tau_1^{+1},u_{1+\frac{1}{2}},\tau_2^{-1},\tau_2^{+1},...,u_{N-\frac{1}{2}},\tau_N^{-1},\tau_N^{+1},u_{N+\frac{1}{2}}),$$

and the right-hand side is

$$(0,-\frac{S_1^{-1}}{2},-\frac{S_1^{+1}}{2},0,-\frac{S_2^{-1}}{2},-\frac{S_2^{+1}}{2},0,...,0,-\frac{S_{N-1}^{-1}}{2},-\frac{S_{N-1}^{+1}}{2},0,-\frac{S_N^{-1}}{2},-\frac{S_N^{+1}}{2},0).$$

There are no external toroidial forces. The driving effect comes from the nontrivial coefficients S_i^{-1} and S_i^{+1}.

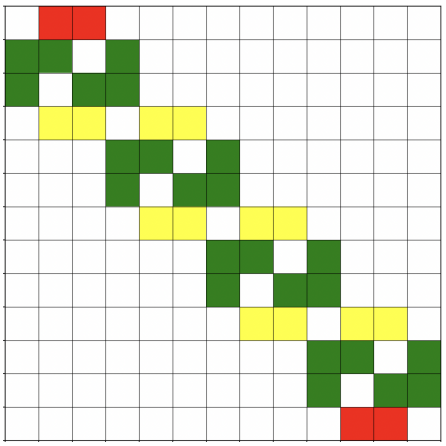


Figure 3.7 Structure of the band matrix of size $(3N+1)^2$ for the toroidal system of deformation equations with $N = 4$ with a bandwidth of 2. The different colours correspond to different types of equations: rheology equations (green), boundary conditions (red), and equations of motion (yellow).

3.6 Calculation of the Dissipation

In this section, we focus in more detail on the calculation of dissipation. As mentioned previously, we need to calculate the dissipative heat source $h(t, x)$ while solving the deformation equation so that it can be used in the heat equation. We simulate the deformation until it reaches a converged state, and then we compute the dissipation as an average over a period. There are two different types of dissipation to be calculated. First, we need to determine the (density of) dissipation as a function of coordinates:

$$\overline{h}(x) = \frac{1}{T_p} \int_0^{T_p} h(t', x) dt', \tag{3.37}$$

which serves as a source term in the heat equation. Additionally, it is useful to calculate the total dissipation as the integral of the dissipation density:

$$H_t = \frac{1}{T_p} \int_0^{T_p} \int_\Omega h(t', x) dx dt', \tag{3.38}$$

also averaged over the period. These two quantities can be computed in different ways. It is much easier to determine the total dissipation. We do so by inserting the harmonic expansions of the tensors into the dissipation formula 2.4 and using the orthonormality of the spherical tensors.

Let us denote by q^{l2}_{jm} the coefficients of the deviatoric tensor, which represents the product of the deviatoric Cauchy stress tensor and the fluidity. We compute this tensor at every time step and at every layer to update the integral in Maxwell's rheology. The approximate formula for the total dissipation can then be written as:

$$H_t = \frac{1}{2N} \sum_{i=1}^{N} \int_{R_{\text{bot}}}^{R_{\text{bot}}+d} \left[\sum_{j=0}^{j_{\max}} \sum_{m=0}^{j} \sum_{l=|j-2|}^{j+2} (2 - \delta_{m0}) \Big(\operatorname{Re}(q^{l2}_{jm}(t_i, r)) \operatorname{Re}(\tau^{l2}_{jm}(t_i, r)) \right.$$
$$\left. + \operatorname{Im}(q^{l2}_{jm}(t_i, r)) \operatorname{Im}(\tau^{l2}_{jm}(t_i, r)) \Big) \right] r^2 \, dr, \tag{3.39}$$

where it approximately holds that N timesteps correspond to one period. The term $(2 - \delta_{m0})$ accounts for the coefficients of negative orders $-m$. The integral over the radial variable r is further approximated using the trapezoidal rule with discrete layer values:

$$\int_{R_{\text{bot}}}^{R_{\text{bot}}+d} f(r)dr \approx \sum_{i=1}^{N-1} \frac{\Delta r}{2}\Big(f(r_i) + f(r_{i+1})\Big). \tag{3.40}$$

Calculating the spatially dependent volumetric dissipation is more challenging. To achieve this, we need to compute:

$$h(t,x) = \frac{1}{2\eta(T(t,x))}\Bigg[\tau^D_{xx}(t,x)\tau^D_{xx}(t,x) + \tau^D_{yy}(t,x)\tau^D_{yy}(t,x) + \tau^D_{zz}(t,x)\tau^D_{zz}(t,x) + 2\Big(\tau^D_{xy}(t,x)\tau^D_{xy}(t,x) + \tau^D_{xz}(t,x)\tau^D_{xz}(t,x) + \tau^D_{yz}(t,x)\tau^D_{yz}(t,x)\Big)\Bigg], \tag{3.41}$$

where τ^D_{xx}, τ^D_{yy}, etc., denote the Cartesian components of the deviatoric Cauchy stress tensor. We made use of the tensor's symmetry by combining the off-diagonal terms in pairs. We further expand the tensor components in a spherical harmonic series at discrete radial layers:

$$h(t, r_i, \theta, \phi) = \sum_{j=0}^{j_{\max}} \sum_{m=-j}^{j} h_{jm}(t, r_i) Y_{jm}(\theta, \phi). \tag{3.42}$$

To compute the dissipation, we first calculate the Cartesian components of the deviatoric Cauchy stress tensor. Instead of computing them directly, we first evaluate the traction vectors $\boldsymbol{\tau}_x = \boldsymbol{\tau}^D \cdot \mathbf{e}_x$, $\boldsymbol{\tau}_y = \boldsymbol{\tau}^D \cdot \mathbf{e}_y$, and $\boldsymbol{\tau}_z = \boldsymbol{\tau}^D \cdot \mathbf{e}_z$, and then extract their Cartesian components by projecting them again onto the corresponding Cartesian directions. There is an analytical way to compute these scalar products with the Cartesian basis vectors using formulas in Section A.2.7, which involve Clebsch-Gordan coefficients and Wigner 6j symbols. This allows us to compute the Cartesian components of the deviatoric stress analytically. We then evaluate these components, along with viscosity, on the grid and use them to compute the dissipation field using equation (3.41). Finally, we convert the grid values of dissipation back into spherical harmonic coefficients.

3.7 The Heat Equation in the Spherical Representation

In this section, we present the heat equation in its spherical harmonic representation and explain how we solve it using discretised radial layers and time steps. The heat equation is written as

$$\rho_i c_p \frac{\partial T(t,x)}{\partial t} = k_0 \nabla \cdot \left(\frac{1}{T(t,x)} \nabla T(t,x)\right) + h(t,x), \tag{3.43}$$

where we have substituted the nonlinear conductivity (2.3). The trick to handling this nonlinearity is that we can use the derivative formula for logarithm and rewrite it as

$$\rho_i c_p \frac{\partial T(t,x)}{\partial t} = k_0 \Delta \ln\Big(T(t,x)\Big) + h(t,x). \tag{3.44}$$

The spectral method again involves substituting the harmonic series expansion for all functions, which means we also need the harmonic expansion of the logarithm of temperature:

$$\ln\Big(T(t,r_i,\theta,\phi)\Big) = \sum_{j=0}^{j_{\max}} \sum_{m=-j}^{j} (\ln T)_{jm}(t,r_i) Y_{jm}(\theta,\phi), \tag{3.45}$$

where we compute the coefficients by evaluating the temperature on a grid, applying the logarithm pointwise, and then projecting the resulting values back onto spherical harmonics. This procedure is repeated at each time step and for every radial layer.

By plugging in the harmonic expansion, using the orthogonality property, and applying the formula for the action of the Laplace operator (A.57a), we obtain the heat equation for the harmonic coefficients in the form

$$\begin{aligned}\frac{\partial T_{jm}(t,r)}{\partial t} = \frac{k_0}{\rho_i c_p}\Bigg(&\frac{d^2(\ln T)_{jm}(t,r)}{dr^2} + \frac{2}{r}\frac{d(\ln T)_{jm}(t,r)}{dr} \\ &- \frac{j(j+1)}{r^2}(\ln T)_{jm}(t,r)\Bigg) + \frac{h_{jm}(t,r)}{\rho_i c_p}.\end{aligned} \tag{3.46}$$

After applying radial discretisation and approximating the derivatives using finite differences, we obtain

$$\begin{aligned}\frac{\partial T_{jm}(t,r_{i+\frac{1}{2}})}{\partial t} = \frac{k_0}{\rho_i c_p}\Bigg(&\frac{(\ln T)_{jm}(t,r_{i+\frac{3}{2}}) - 2(\ln T)_{jm}(t,r_{i+\frac{1}{2}}) + (\ln T)_{jm}(t,r_{i-\frac{1}{2}})}{(\Delta r)^2} \\ &+ \frac{1}{r}\frac{(\ln T)_{jm}(t,r_{i+\frac{3}{2}}) - (\ln T)_{jm}(t,r_{i-\frac{1}{2}})}{\Delta r} \\ &- \frac{j(j+1)}{r^2}(\ln T)_{jm}(t,r_{i+\frac{1}{2}})\Bigg) \\ &+ \frac{1}{2\rho_i c_p}\left(h_{jm}(t,r_i) + h_{jm}(t,r_{i+1})\right).\end{aligned} \tag{3.47}$$

To simplify the notation, we introduce a function $f_i(t)$ as

$$\frac{\partial T_{jm}(t,r_{i+\frac{1}{2}})}{\partial t} = f_{i+\frac{1}{2}}(t), \tag{3.48}$$

which transforms the problem into an ordinary differential equation in time for the harmonic coefficients $T_{jm}(t,r_{i+\frac{1}{2}})$ at the midlayer $i+\frac{1}{2}$. We solve this equation using the second-order Adams-Bashforth multistep method, where we compute the coefficient at time step $n+2$ as

$$T_{jm}(t_{n+2},r_{i+\frac{1}{2}}) = T_{jm}(t_{n+1},r_{i+\frac{1}{2}}) + \frac{3}{2}\Delta t f_{i+\frac{1}{2}}(t_{n+1}) - \frac{1}{2}\Delta t f_{i+\frac{1}{2}}(t_n). \tag{3.49}$$

Since this is a multistep method, we must retain coefficients from at least one previous step in memory to apply this numerical scheme. The first step is performed using a simple Euler method.

We solve a Dirichlet boundary value problem as introduced in the second chapter, meaning that we have two fixed harmonic series, one at the bottom layer:

$$T_b(\theta,\phi) = \sum_{j=0}^{j_{\max}} \sum_{m=-j}^{j} T^b_{jm} Y_{jm}(\theta,\phi), \tag{3.50}$$

which is very simple, with only the constant term T^b_{00} being nonzero, and one at the top layer:

$$T_t(\theta,\phi) = \sum_{j=0}^{j_{\max}} \sum_{m=-j}^{j} T^t_{jm} Y_{jm}(\theta,\phi). \tag{3.51}$$

These two functions remain fixed throughout the simulation, and we solve the heat equation (3.47) in the middle layers $r_{1+\frac{1}{2}}, ..., r_{N-\frac{1}{2}}$ and after each time step we update the coefficient at the outer mid-layers $r_{\frac{1}{2}}, r_{N+\frac{1}{2}}$, so that the average of the temperature coefficients at first and second mid-layers is equal to the bottom dirichlet condition and similarily the last and last but one equal to the upper dirichlet condition. This way we satisfy the boundary conditions. The choice of initial condition is not very important, as the time evolution is not truly physical—we are mainly interested in the converged stationary solution. One possible choice is to use an initial condition given by a harmonic series, with coefficients obtained via linear interpolation between the two boundary values. Alternatively, we can use as an initial condition the final converged state from a previous simulation run with different parameter values of η_0 and d.

4 Results

In this chapter, we present the results of our simulations. We investigated the effect of tidal dissipation on the spatial temperature distribution, the total heat flux, and the spatial distribution of heat flux at the bottom and top boundaries in the converged state of the system of equations (2.1). Our primary focus is on the role of two parameters: the reference viscosity η_0 at the ice-ocean boundary in the viscosity relation (2.2), and the geometric parameter d, the thickness of the ice shell. We consider the viscosity parameter η_0 in the interval $(5\times10^{13}, 1\times10^{16})$ Pa·s. Values below 5×10^{13} Pa·s correspond to unrealistically small ice grains [7], and at very high values like 1×10^{16} Pa·s, the shell behaves almost purely elastically. Due to significant uncertainty in the ice shell thickness, we consider d in the interval $(10, 50)$ km. In all simulations, we used 100 radial layers, which seemed to provide good enough resolution, as seen in the smoothness of the radially dependent functions. For the lateral resolution, we mostly used the spherical harmonic cutoff $j_{\max} = 30$, which worked well in the non melting scenarios, it provided enough resolution and the spectral coefficients converged quickly to zero for higher j. We also tried increasing the resolution up to degree 60 when modeling melting scenarios, but even that did not help resolve those cases successfully.

4.1 Results for the Fixed Parameter $d = 30\,\mathrm{km}$

We begin by presenting detailed results from simulations with a fixed shell thickness of $d = 30$ km and varying viscosity η_0. We compare the results for different viscosities η_0 to a reference case of a purely elastic shell without any dissipation, which we denote by $\eta_0 = +\infty$. Table 4.1 summarizes the total tidal heating in the ice shell, the total inner heat flux from the ocean to the shell, and the total outer heat flux at the surface. For the parameter value $\eta_0 = 5 \times 10^{13}$ Pa·s, the ice shell undergoes melting, the temperature exceeds 273 K, the melting point of the ice. We attempted to handle these melting scenarios by introducing a temperature cap at the melting point, but were not able to make it converge. We can see that the tidal heating plus inner flux equals the outer flux, as it should, so that energy is conserved. The case $\eta_0 = +\infty$ corresponds to a fully elastic shell, where there is no tidal heating and the outer flux equals the inner flux.

We have also made another series of simulations with the same parameters, but without the self-gravity potential, to compare the results. The corresponding values for this model are shown in Table 4.2. As expected, the tidal dissipation is weaker without self-gravity. The ice shell is not melting for any of those η_0 values for this model.

Figure 4.1 shows heat map plots of the steady state temperature field at a fixed radial distance, approximately 2.15 km above the ice–ocean boundary. The precise distance is not all that important and is related to the discretization; what matters is that it lies slightly above the bottom boundary, where the dissipation is strongest. These plots are shown for three different values of the reference viscosity parameter η_0: 1×10^{15}, 5×10^{14}, and 1×10^{14} Pa·s. In each row, the left plot shows the absolute temperature field, while the right plot displays the difference between the temperature field at the given η_0 and the reference no-heating case

η_0 [Pa·s]	Tidal heating [GW]	Inner flux [GW]	Outer flux [GW]
$+\infty$	0	721.47	721.47
1×10^{16}	4.1	717.5	721.6
5×10^{15}	8.2	713.5	721.7
1×10^{15}	41.7	681.2	722.9
5×10^{14}	83.8	640.6	724.4
1×10^{14}	330.5	408.3	738.8
5×10^{13}	– melting	–	–

Table 4.1 Total tidal heating in the ice shell and total heat fluxes at the inner and outer boundaries, for simulations with fixed shell thickness $d = 30$ km and varying reference viscosity η_0. For the lowest viscosity $\eta_0 = 5 \times 10^{13}$ Pa·s, the temperature exceeds the melting point, and the shell becomes unstable due to melting.

η_0 [Pa·s]	Tidal heating [GW]	Inner flux [GW]	Outer flux [GW]
$+\infty$	0	721.47	721.47
1×10^{16}	2.7	718.9	721.6
5×10^{15}	5.4	716.2	721.7
1×10^{15}	27.5	694.9	722.4
5×10^{14}	54.6	668.8	723.4
1×10^{14}	193.8	537.0	730.8
5×10^{13}	250.0	487.6	737.6

Table 4.2 Total tidal heating in the ice shell and total heat fluxes at the inner and outer boundaries for simulations with fixed shell thickness $d = 30$ km and varying reference viscosity η_0, without self-gravity.

($\eta_0 = \infty$).

We now present plots of radial temperature dependence at selected spherical angles, shown in Figure 4.2. The angles include the north pole $(0°, 0°)$, the position $(30°, 90°)$, which appears to correspond approximately to the location of peak dissipation, the equator at zero longitude $(90°, 0°)$, and the equator at $(90°, 90°)$. In the left column of each row, we display the absolute temperature profiles as functions of depth. In the right column, we show the difference between each case and the reference no-heating case. Each plot contains multiple curves for different values of the viscosity parameter η_0.

Further, in Figure 4.3, the spatial distribution of volumetric dissipation (heat generation) is shown at the same depth, 2.5 km above the ice-ocean boundary, as in the temperature maps in Figure 4.1, for varying values of the viscosity parameter η_0.

Another set of plots, shown in Figure 4.4, presents the spatial distribution of the heat flux at the lower boundary of the ice shell. As before, the left column shows the total heat flux fields for different values of the viscosity parameter η_0, while the right column displays the difference from the no-heating reference case ($\eta_0 = \infty$). Similarly, Figure 4.5 shows the corresponding heat flux distributions at the upper boundary of the shell. The plots illustrate how the surface and basal heat flux patterns evolve with increasing tidal dissipation due to lower viscosities.

4.2 Results for Other Values of Thickness d

Next, we explore the parameter space more broadly by varying both the viscosity parameter η_0 and the shell thickness d. Figure 4.6 shows the total tidal dissipation in the ice shell and the total heat fluxes at the boundaries as functions of these two parameters. These values are obtained by interpolating the grid data. The first plot shows the total tidal dissipation in Europa's ice shell, while the second and third show the total heat flux at the bottom and top of the shell. In the figures, a red dashed line indicates the combinations of parameters where the ice starts to melt. Bellow this line, the solution is no longer physically valid, since our model doesn't account for melting.

Further, we show in Figure 4.7 the heat flux distribution at the upper boundary of the ice shell for various combinations of reference viscosity η_0 and shell thickness d. Each row corresponds to a different viscosity $(1\times10^{15}, 5\times10^{14}, 1\times10^{14}, 5\times10^{13})$ Pa·s, and each column to a shell thickness $(10, 30, 50)$ km. This layout allows for a direct comparison of how changes in these parameters influence the surface heat flux patterns. For certain parameter combinations, the solution becomes unphysical due to partial melting of the ice shell, those panels are intentionally left blank.

Similarly, in Figure 4.8, we present the heat flux distribution at the inner boundary of the ice shell, that is, the heat entering the shell from the underlying ocean. The layout follows the same structure as Figure 4.7: each row corresponds to a different viscosity $(1\times10^{15}, 5\times10^{14}, 1\times10^{14}, 5\times10^{13})$ Pa·s, and each column to a shell thickness $(10, 30, 50)$ km. Blank panels indicate simulations where partial melting occurred.

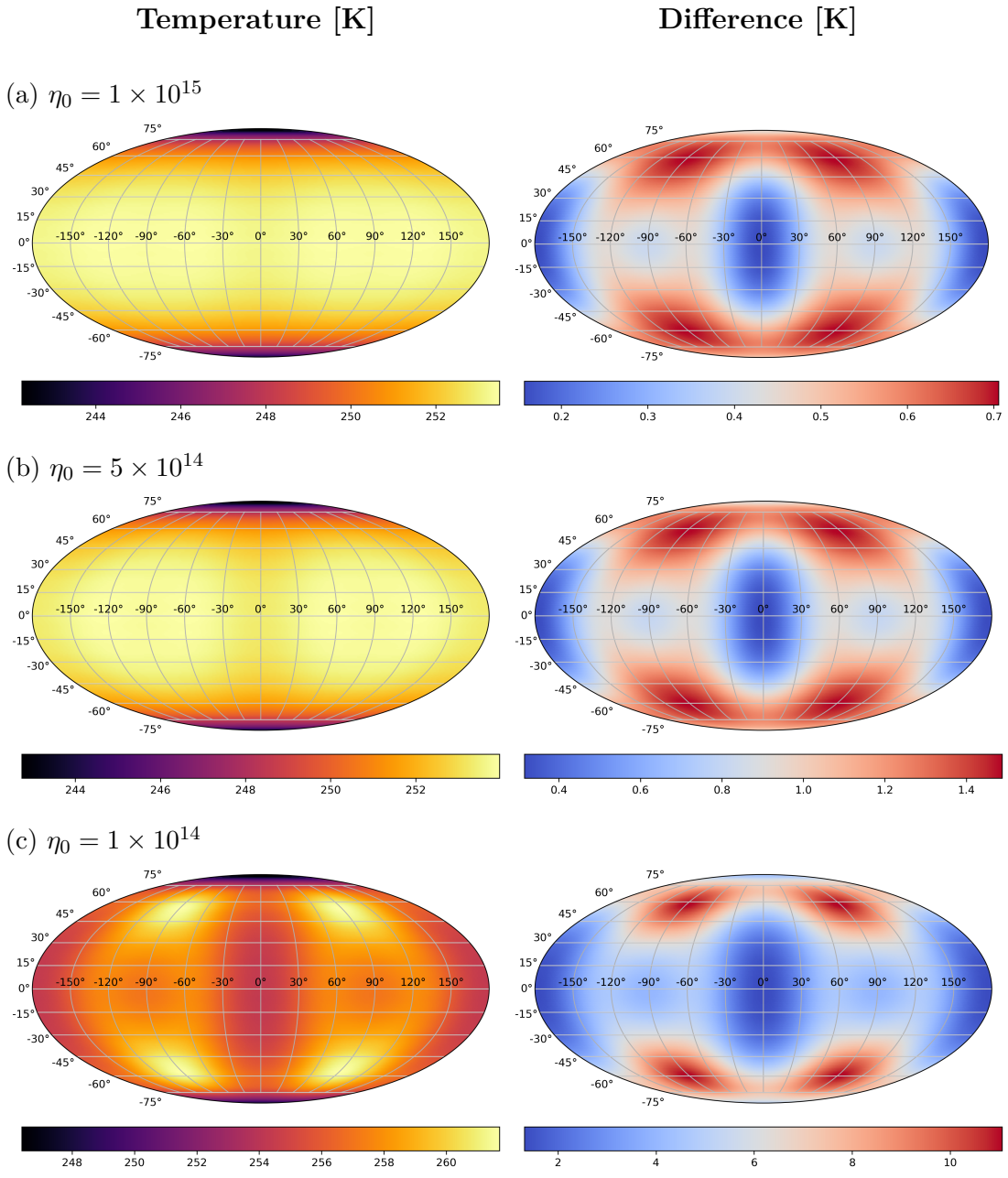


Figure 4.1 Temperature field at a fixed depth (2.15 km above the ice-ocean boundary) for different reference viscosities η_0, assuming a fixed ice shell thickness of $d = 30$ km. Left: total temperature distribution. Right: difference from the reference case with no tidal heating ($\eta_0 = \infty$).

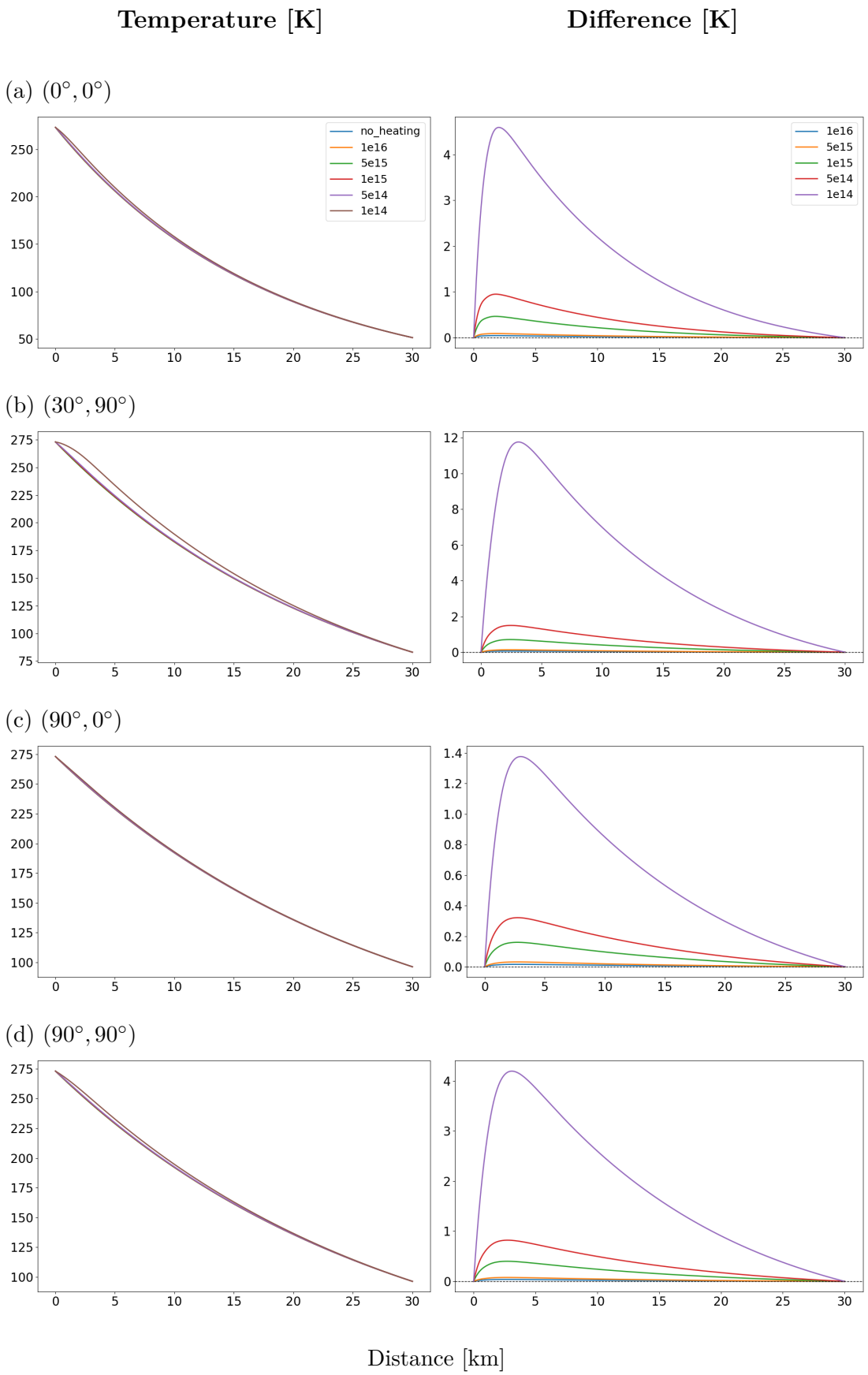


Figure 4.2 Temperature profiles along the radial direction for selected colatitude–longitude combinations, assuming a fixed ice shell thickness of $d = 30$ km. Left: total temperature distribution. Right: difference from the reference case with no tidal heating ($\eta_0 = \infty$).

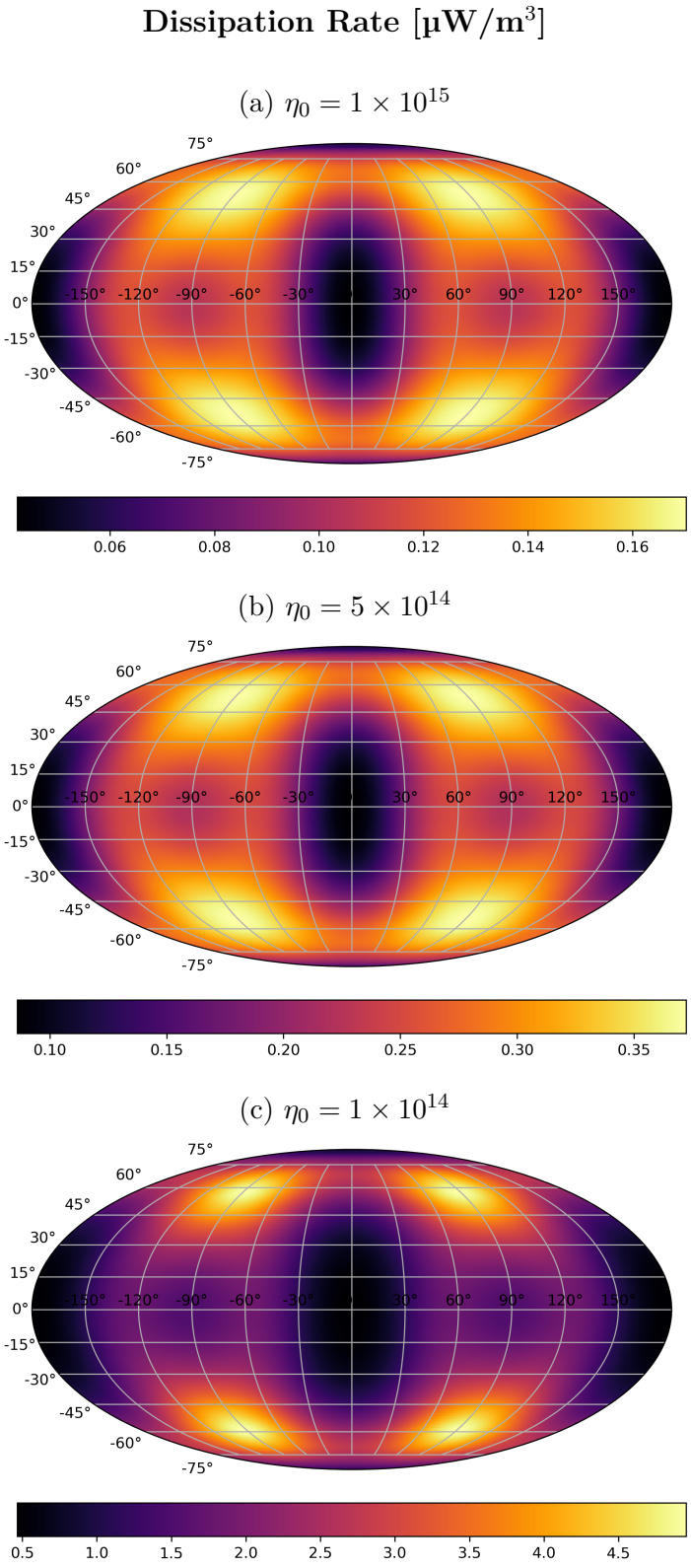


Figure 4.3 Volumetric dissipation distribution at a fixed depth (2.5 km above the ice-ocean boundary) for different reference viscosities η_0, assuming a fixed ice shell thickness of $d = 30$ km.

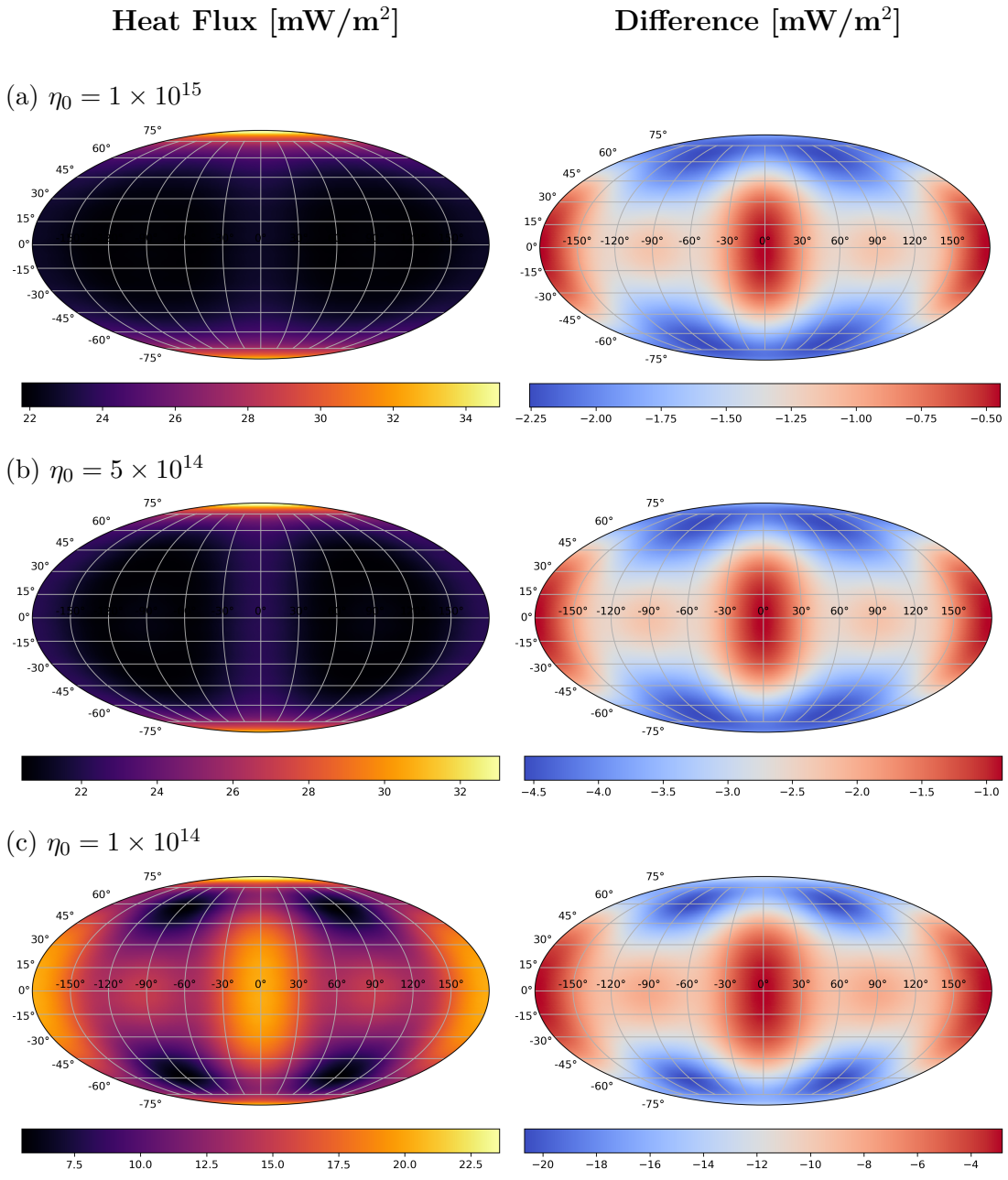


Figure 4.4 Heat flux distribution at the lower boundary of the shell for different reference viscosities η_0, assuming a fixed ice shell thickness of $d = 30$ km. Left: total heat flux entering the shell. Right: difference from the reference case with no tidal heating ($\eta_0 = \infty$).

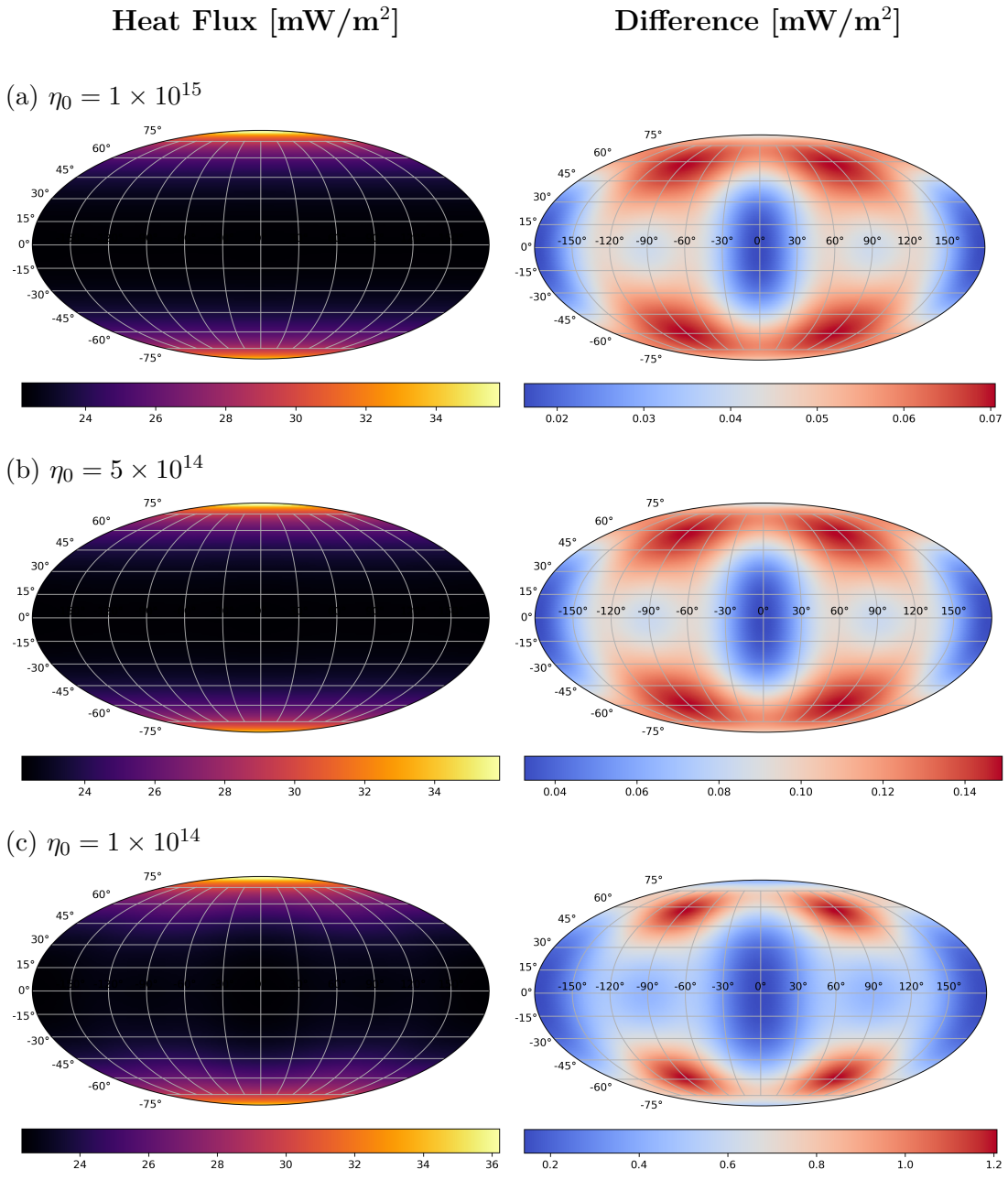


Figure 4.5 Surface heat flux distribution at the upper boundary of the shell for different reference viscosities η_0, assuming a fixed ice shell thickness of $d = 30$ km. Left: total outgoing heat flux. Right: difference from the reference case with no tidal heating ($\eta_0 = \infty$).

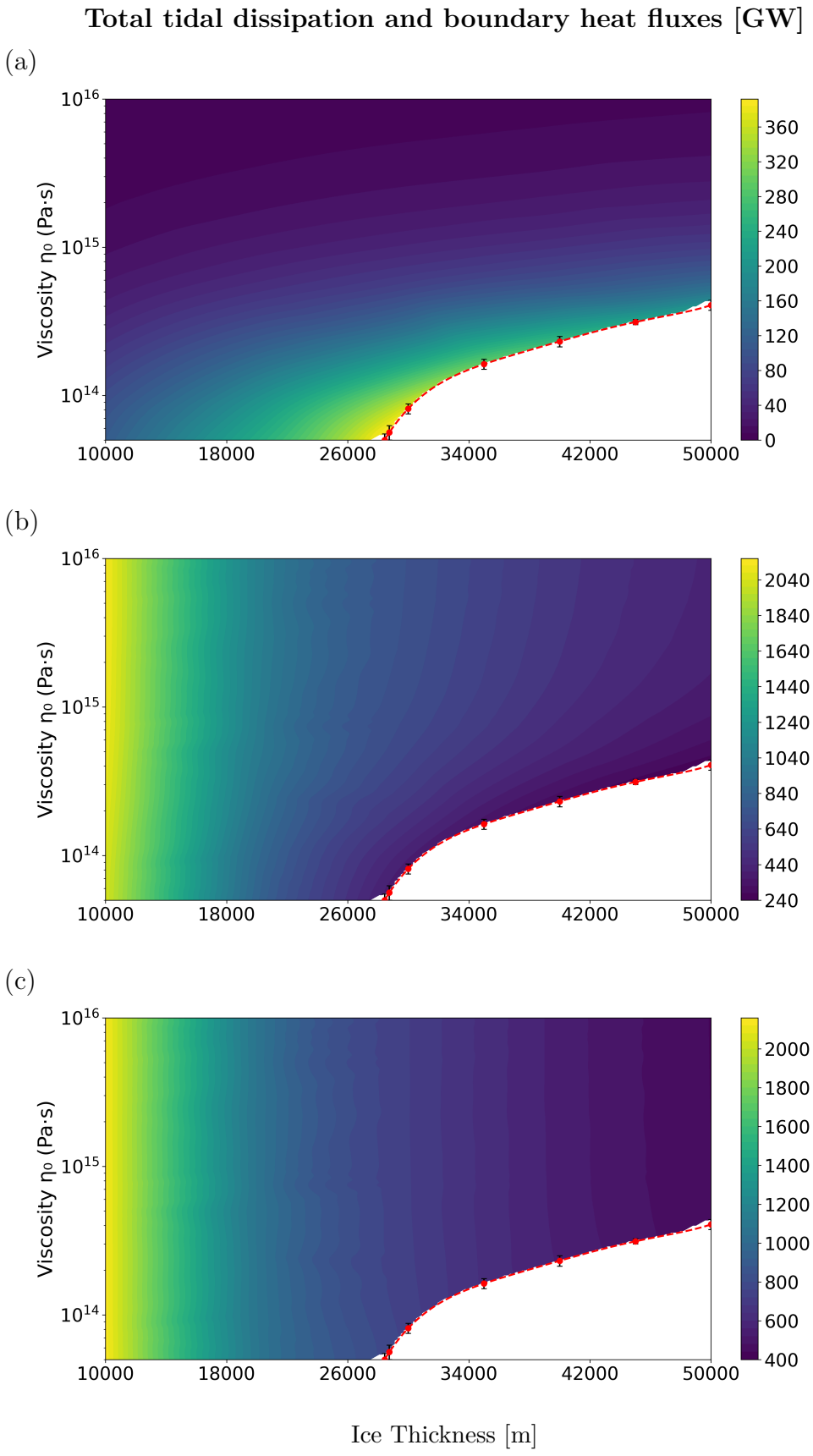


Figure 4.6 (a) Total tidal dissipation, (b) total heat flux at the lower boundary, and (c) total heat flux at the upper boundary, as functions of the shell thickness d and reference viscosity η_0. The red dashed line in each panel indicates where melting begins.

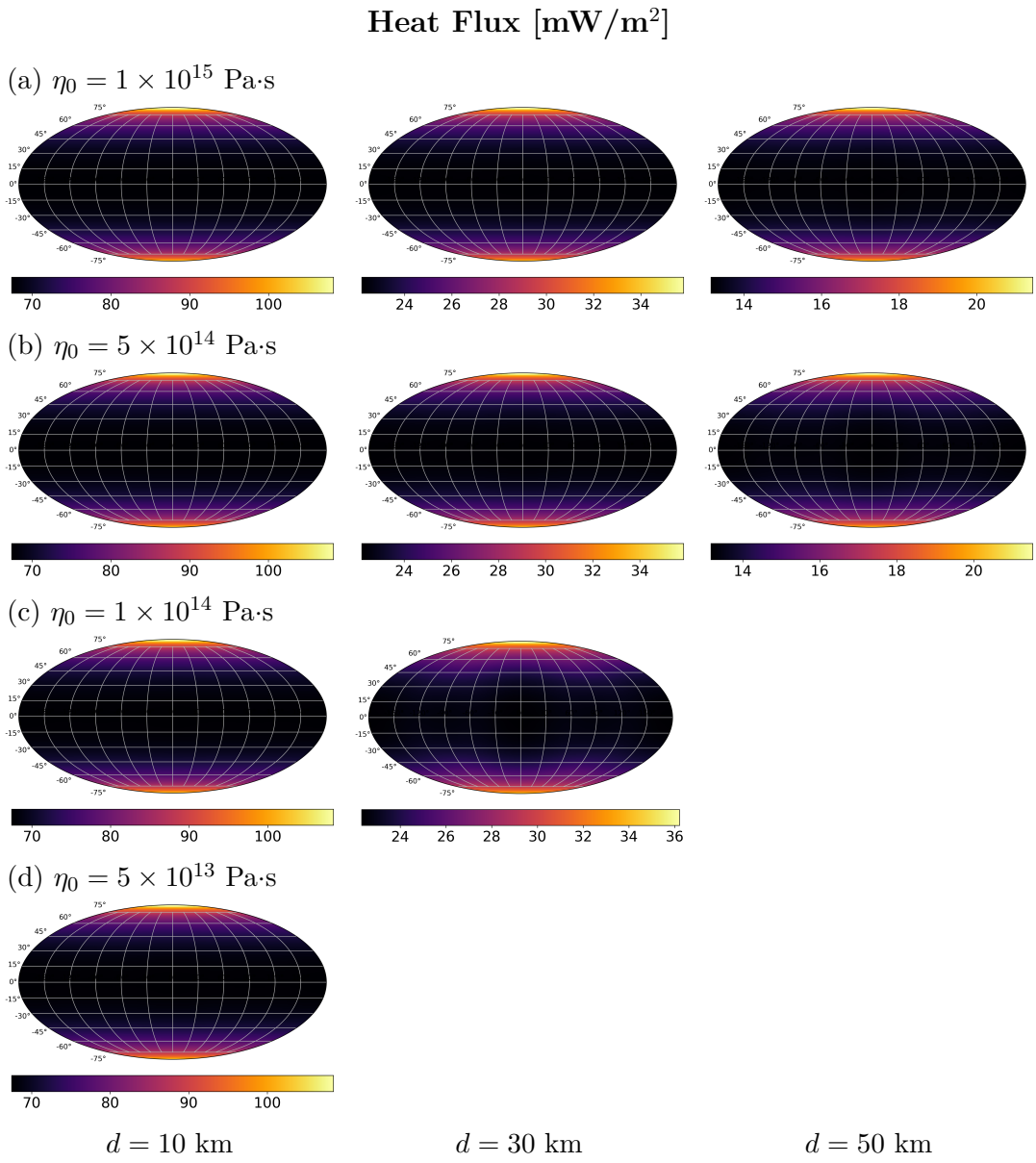


Figure 4.7 Surface heat flux distribution at the upper boundary of the ice shell for various combinations of shell thickness d and reference viscosity η_0. Each row corresponds to a different viscosity $(1 \times 10^{15}, 5 \times 10^{14}, 1 \times 10^{14}, 5 \times 10^{13})$ Pa·s, and each column to a shell thickness $(10, 30, 50)$ km. Panels without data are left blank, as the corresponding simulations led to partial melting, making the results unphysical.

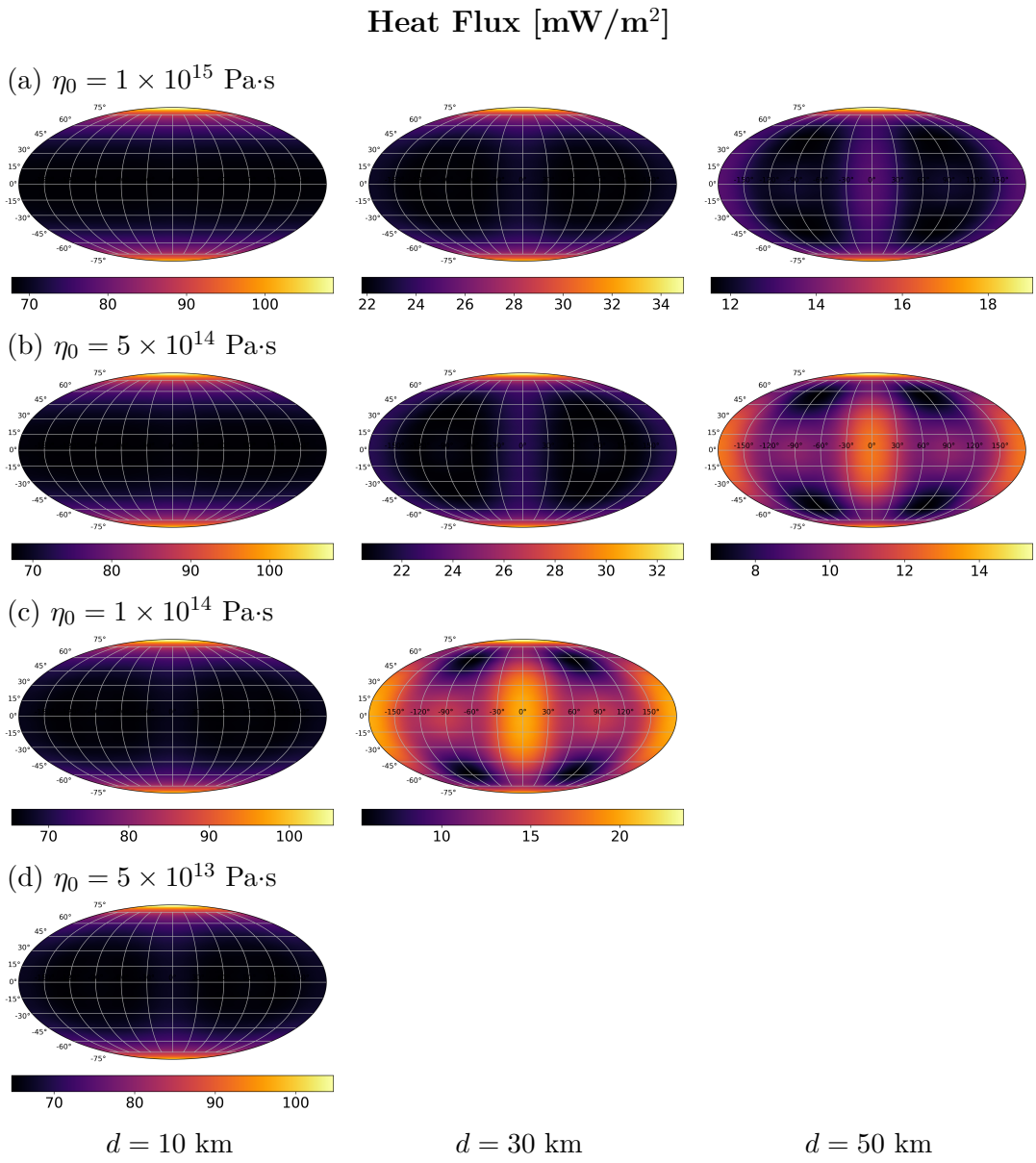


Figure 4.8 Heat flux distribution at the inner boundary of the ice shell (ice–ocean interface) for various combinations of shell thickness d and reference viscosity η_0. Each row corresponds to a different viscosity $(1 \times 10^{15}, 5 \times 10^{14}, 1 \times 10^{14}, 5 \times 10^{13})$ Pa·s, and each column to a shell thickness $(10, 30, 50)$ km. Blank panels correspond to simulations where partial melting made the results unphysical.

Discussion and Conclusions

In this final section, we discuss in detail the results obtained from the modeling presented in Section 4. We explain the main features of the output data and attempt to interpret them physically. We also address the initial research questions and discuss the limitations of our model.

Starting with Table 4.2 and the total dissipation and heat flux functions in Figure 4.6, we see that tidal dissipation can generate a significant amount of heat. This dissipation depends on the reference viscosity parameter η_0, the higher the η_0, the greater the dissipation. This is expected, since viscosity describes how much a material behaves non-elastically, how effectively it dissipates forces into heat. Near the edge of stability, when the ice is close to melting, the total dissipation can reach nearly the same value as the total inner heat flux. For example, for $d = 30$ km, dissipation accounts for up to 93% of the total heat entering from the ocean. In such cases, nearly half of the heat needed to maintain a stationary state could be generated tidally within the ice shell, while the other half must come from the ocean, either also tidally generated or due to other sources like radiogenic heating from the mantle.

We also identified boundary values, a curve in the (η_0, d) parameter space, where the model becomes unstable due to excessive tidal heating, causing the temperature to exceed the melting point of ice (273 K) near the ice-ocean boundary. The smallest thickness d for which this happens at $\eta_0 = 5 \times 10^{14}$ Pa·s is approximately 28 km. For greater thicknesses, melting occurs at smaller η_0, as expected, since the cooling effect from the outer boundary becomes weaker with increasing shell thickness. For example, at $d = 50$ km, melting occurs already at $\eta_0 = 4 \times 10^{14}$ Pa·s. Most of the data can be interpreted as an interplay between two effects, tidal heating within the domain and cooling from the upper boundary, described by the Dirichlet condition.

The heating is strongly localized, as seen in Figure 4.3, and becomes even more localized for larger viscosities. If viscosity were constant, experiments show that heating would be strongest at the poles, where tidal forces are most intense. However, since viscosity in our model is temperature-dependent and the poles are cooled most effectively by the boundary condition, their temperature, and hence viscosity, is lower. As a result, the maximum of tidal dissipation shifts to approximately 90 degrees colatitude and 60 degrees longitude, with symmetric counterparts. This pattern appears largely independent of η_0 and d, which mainly influence the amplitude of heating. These same regions are also where melting starts for critical parameter values, as the heating has the strongest influence on the temperature distribution there, as seen in Figures 2.2 and 4.2. This is clearest in the radial profiles in Figure 4.2, where the profiles for other angles resemble the no-heating case, except at the (30, 90) angle combination, where a more substantial change in temperature is observed.

Tidal heating significantly affects the influx of heat from the ocean at the lower boundary, both the total flux (see Figure 4.6) and the spatial distribution (Figures 4.4 and 4.8). The lowest heat flow is observed precisely at the (30, 90) angles and their symmetric counterparts, which coincide with the strongest dissipation. In contrast, tidal heating has very little effect on the heat flux at

the outer boundary. The total surface heat flux remains almost the same, only slightly larger with tidal heating, and the spatial distributions are nearly identical, as shown in Figures 4.5 and 4.7. The heat flux is still strongest at the poles and weakest at the equator, consistent with the imposed surface temperature boundary condition. Thus, the surface flux is governed mainly by this boundary condition, with inner heating having almost no effect. The dissipation is strongest near the lower boundary, where the temperature is highest and the ice most viscous. This localized heat is then conducted upward through the shell, where it becomes smoothed out by the diffusion process, eliminating any localized structure in the heat flux at the surface.

There are several limitations to our model. We made a number of approximations and assumptions. One is that we assumed a laterally uniform ice shell thickness, independent of position. While this may be a reasonable simplification, since there may be smoothing mechanisms operating on the surface, it ignores possible variations in shell geometry. Another approximation is the use of Maxwell rheology. While the Maxwell model is useful, tractable, and often accurate, the Andrade rheology has been shown to describe ice behavior better. However, Andrade is significantly more difficult to implement. Beyond rheology, the overall assumption of seeking a stationary solution is itself questionable. The reality is likely quasistatic or periodic, particularly when combined with melting dynamics. In reality, ice may melt in some regions and freeze in others, with material being transported within the shell from freezing to melting zones. We also modeled the shell as homogeneous, assuming the same grain size everywhere and ignoring the effects of fractures or impurities. Finally, we applied a simplified boundary temperature distribution using a Dirichlet condition. In reality, surface temperature is likely not symmetric around the equator due to spatial variations in albedo.

Nonetheless, we believe that our model strikes a reasonable balance between physical realism and computational complexity. While our results may not constitute cutting-edge science, we hope they make a small but nontrivial contribution to the broader effort of understanding the structure and evolution of icy moons. Perhaps the most interesting aspect of the model is the interplay between the imposed surface temperature condition and the internal tidal heating. We have identified the regions where heating is strongest near the lower boundary, the curve in parameter space where melting begins, and the impact of tidal heating on the boundary heat fluxes. The internal heat flux is significantly affected by tidal dissipation, while the surface heat flux remains largely unaffected by internal heating.

A Appendix

A.1 Comment on Uniqueness of the Stationary Solution

In this thesis, we mainly focus on the technical and implementation aspects of how to find the stationary solution of the system of equations (2.1). In this section, we briefly comment on the uniqueness of this stationary solution. In the PDE analysis community, people often talk about the so-called well-posedness of a problem, which means that a solution exists, is unique, and depends continuously on the initial and boundary data. This provides an analytical guarantee that it actually makes sense to search for a solution. It would be great to show such a property for the system (2.1), and in particular, we are interested in the uniqueness of the stationary temperature distribution. However, proving such results can be very difficult for complex nonlinear problems, and so in physics, where equations often become highly nonlinear and complicated, these types of results are often left out. In physics, there is at least the belief that the equations should reflect reality, so if a solution didn't exist, it would probably mean that something is fundamentally wrong with the model, since in nature, the solution clearly exists.

In this section, we try to prove the uniqueness of the stationary temperature field for progressively more complicated versions of the system (2.1). We start with the simple linear heat equation with constant heating, then add the nonlinearity in the conductivity (2.3), and finally include the nonlinearity in the heating term (2.4). For each of these cases, we are able to show uniqueness. In the case with nonlinear conductivity, we identify an additional condition that ensures coercivity and is necessary for the uniqueness proof. This means that if the viscosity field in the Maxwell rheology (2.7) were given and not dependent on temperature, and if the only nonlinearities were in the conductivity and the heating, we would have uniqueness. Although this is still a significant simplification, the temperature dependence of viscosity in the rheology is probably the most interesting feature of the full model, as it couples deformation with heat conduction, but we still think this is a nice result. The proofs are not fully rigorous in terms of functional analysis (e.g., we do not work in Sobolev spaces), but we believe they could be made rigorous with some extra effort.

A.1.1 Uniqueness of the Stationary Heat Equation with Linear Conductivity

We consider the stationary heat equation with a fixed heat source and constant conductivity $k > 0$

$$-k\Delta T + h = 0 \quad \text{in } \Omega, \qquad T = T_b \quad \text{on } \partial\Omega.$$

Assume that T_1 and T_2 are two solutions of this boundary value problem. Then their difference $\delta T = T_1 - T_2$ satisfies:

$$-k\Delta \delta T = 0 \quad \text{in } \Omega, \qquad \delta T = 0 \quad \text{on } \partial\Omega.$$

We multiply the equation by δT and integrate over Ω:

$$k \int_\Omega (-\Delta \delta T)\, \delta T \, dx = 0.$$

By integration by parts and using the homogeneous Dirichlet boundary condition $\delta T = 0$ on $\partial\Omega$, we obtain:

$$\int_\Omega |\nabla \delta T|^2 \, dx = 0.$$

This implies $\nabla \delta T = 0$ in Ω, i.e., δT is constant in Ω. The boundary condition $\delta T = 0$ on $\partial\Omega$ then implies $\delta T = 0$ everywhere. Thus:

$$T_1 = T_2 \quad \text{in } \Omega.$$

A.1.2 Uniqueness of the Stationary Heat Equation with Nonlinear Conductivity

Now we consider the stationary heat equation with temperature-dependent conductivity (2.3) with given heating h

$$-\nabla \cdot \left(\frac{k_0}{T} \nabla T \right) + h = 0 \quad \text{in } \Omega, \qquad T = T_b \quad \text{on } \partial\Omega,$$

where $T > 0$. Let T_1 and T_2 be two solutions corresponding to the same boundary data and source term h. Subtracting the two equations yields:

$$\nabla \cdot \left(\frac{1}{T_1} \nabla T_1 - \frac{1}{T_2} \nabla T_2 \right) = 0.$$

Testing this with $T_1 - T_2$, integrating over Ω, and using the boundary condition $T_1 = T_2$ on $\partial\Omega$, we obtain:

$$\int_\Omega \left(\frac{1}{T_1} \nabla T_1 - \frac{1}{T_2} \nabla T_2 \right) \cdot \nabla (T_1 - T_2) \, dx = 0.$$

To prove uniqueness, we would need a pointwise coercivity estimate of the form

$$\begin{aligned} &\left(\frac{1}{T_1(x)} \nabla T_1(x) - \frac{1}{T_2(x)} \nabla T_2(x) \right) \cdot (\nabla T_1(x) - \nabla T_2(x)) \\ &\quad \geq C \, |\nabla (T_1(x) - T_2(x))|^2 \quad \text{for all } x \in \Omega, \end{aligned} \tag{A.1}$$

for some constant $C > 0$. If such an estimate holds, then the integrand is pointwise non-negative. Since its integral over Ω is zero, it must hold

$$\int_\Omega |\nabla (T_1 - T_2)|^2 \, dx = 0,$$

which implies $\nabla (T_1 - T_2) = 0$ in Ω, and hence $T_1 - T_2$ is constant. Using the boundary condition $T_1 = T_2$ on $\partial\Omega$, we obtain $T_1 = T_2$ in Ω, proving uniqueness.

Let's now return and try to prove the coercivity estimate (A.1). We observe that in the special case $T_1 = T_2$, the inequality holds trivially with constant $C = 1/T_1(x)$. It would be ideal if the estimate held generally, but unfortunately this is not the case. It is not difficult to construct counterexamples where $T_1 \approx T_2$,

yet the inequality fails. For such cases it holds that the gradient vectors are close to each other in a norm.

To recover coercivity, we impose an additional assumption: a relation between the difference in gradients and the difference in function values. Specifically, we will prove (A.1) under the condition that the gradients $\nabla T_1(x)$ and $\nabla T_2(x)$ are sufficiently separated relative to the function values. We begin by expanding the left-hand side:

$$\left(\frac{1}{T_1(x)}\nabla T_1(x) - \frac{1}{T_2(x)}\nabla T_2(x)\right) \cdot (\nabla T_1(x) - \nabla T_2(x)) =$$
$$= \frac{1}{T_1(x)}|\nabla T_1(x)|^2 + \frac{1}{T_2(x)}|\nabla T_2(x)|^2 - \left(\frac{1}{T_1(x)} + \frac{1}{T_2(x)}\right)\nabla T_1(x) \cdot \nabla T_2(x).$$

To proceed, we assume without loss of generality that $T_1(x) > T_2(x)$. Then we regroup the expression as follows to construct the coercivity term with the smaller constant:

$$\begin{aligned}
&= \frac{1}{T_1(x)}\left(|\nabla T_1(x)|^2 - 2\nabla T_1(x) \cdot \nabla T_2(x) + |\nabla T_2(x)|^2\right) + \\
&\quad + \left(\frac{1}{T_2(x)} - \frac{1}{T_1(x)}\right)|\nabla T_2(x)|^2 - \left(\frac{1}{T_2(x)} - \frac{1}{T_1(x)}\right)\nabla T_1(x) \cdot \nabla T_2(x) \\
&= \frac{1}{T_1(x)}|\nabla T_1(x) - \nabla T_2(x)|^2 + \\
&+ \left(\frac{1}{T_2(x)} - \frac{1}{T_1(x)}\right)\left(|\nabla T_2(x)|^2 - \nabla T_1(x) \cdot \nabla T_2(x)\right).
\end{aligned}$$

This expression separates the positive definite term from the remainder, which we would like to ensure is non-negative. We can even go a bit further: since it's enough for us to have the coercivity constant arbitrarily small but positive, we can isolate an ε-coercive term and proceed as follows:

$$\begin{aligned}
&= \varepsilon|\nabla T_1(x) - \nabla T_2(x)|^2 + \left(\frac{1}{T_1(x)} - \varepsilon\right)|\nabla T_1(x) - \nabla T_2(x)|^2 + \\
&+ \left(\frac{1}{T_2(x)} - \frac{1}{T_1(x)}\right)\left(|\nabla T_2(x)|^2 - \nabla T_1(x) \cdot \nabla T_2(x)\right),
\end{aligned}$$

so if

$$\begin{aligned}
&\left(\frac{1}{T_1(x)} - \varepsilon\right)|\nabla T_1(x) - \nabla T_2(x)|^2 + \\
&+ \left(\frac{1}{T_2(x)} - \frac{1}{T_1(x)}\right)\left(|\nabla T_2(x)|^2 - \nabla T_1(x) \cdot \nabla T_2(x)\right) \geq 0 \quad \text{for all } x, \qquad \text{(A.2)}
\end{aligned}$$

for arbitrarily small $\varepsilon > 0$, then we have the coercivity and hence the uniqueness of the solution. This is the additional assumption that we need to add. It is not obvious how to interpret this condition. Maybe it would be possible to come up with a weaker condition. We can now also reverse the argument and say that if we have two different solutions of the PDE, then they cannot satisfy the condition (A.2).

A.1.3 Uniqueness in the Case of Temperature-Dependent Heating

Finally, we consider the stationary heat equation with both nonlinear conductivity and a temperature-dependent source term:

$$-\nabla \cdot \left(\frac{k_0}{T} \nabla T \right) + h(T) = 0 \quad \text{in } \Omega, \qquad T = T_b \quad \text{on } \partial\Omega.$$

Suppose T_1 and T_2 are two solutions with the same Dirichlet boundary condition $T_1 = T_2$ on $\partial\Omega$. Subtracting the equations gives:

$$-\nabla \cdot \left(\frac{k_0}{T_1} \nabla T_1 - \frac{k_0}{T_2} \nabla T_2 \right) + h(T_1) - h(T_2) = 0.$$

We multiply the equation by $T_1 - T_2$ and integrate over Ω. Integration by parts yields:

$$\int_\Omega \left(\frac{k_0}{T_1} \nabla T_1 - \frac{k_0}{T_2} \nabla T_2 \right) \cdot \nabla (T_1 - T_2)\, dx + \int_\Omega (h(T_1) - h(T_2))(T_1 - T_2)\, dx = 0.$$

Rewriting:

$$\int_\Omega \left(\frac{k_0}{T_1} \nabla T_1 - \frac{k_0}{T_2} \nabla T_2 \right) \cdot \nabla (T_1 - T_2)\, dx = -\int_\Omega (h(T_1) - h(T_2))(T_1 - T_2)\, dx.$$

Now, if the coercivity condition (A.1) derived in the previous section holds pointwise in Ω, then there exists a constant $C > 0$ such that:

$$\left(\frac{1}{T_1(x)} \nabla T_1(x) - \frac{1}{T_2(x)} \nabla T_2(x) \right) \cdot \nabla (T_1(x) - T_2(x)) \geq C |\nabla (T_1(x) - T_2(x))|^2,$$

which implies

$$\int_\Omega \left(\frac{k_0}{T_1} \nabla T_1 - \frac{k_0}{T_2} \nabla T_2 \right) \cdot \nabla (T_1 - T_2)\, dx \geq k_0 C \int_\Omega |\nabla (T_1 - T_2)|^2 dx.$$

Now suppose that the heat source $h(T)$ is monotone increasing. Then,

$$(h(T_1) - h(T_2))(T_1 - T_2) \geq 0 \quad \text{for all } T_1, T_2,$$

so the right-hand side is non-positive:

$$-\int_\Omega (h(T_1) - h(T_2))(T_1 - T_2)\, dx \leq 0.$$

Therefore, combining both inequalities gives:

$$k_0 C \int_\Omega |\nabla (T_1 - T_2)|^2 dx \leq -\int_\Omega (h(T_1) - h(T_2))(T_1 - T_2)\, dx \leq 0,$$

which implies

$$\nabla (T_1 - T_2) = 0 \quad \text{in } \Omega.$$

Since $T_1 = T_2$ on the boundary, we conclude:

$$T_1 = T_2 \quad \text{in } \Omega.$$

Thus, the solution is unique.

This uniqueness holds under the assumption that the source term $h(T)$ is monotone increasing, as is the case for tidal dissipation modeled by an Arrhenius-type viscosity law:

$$h(T) = Ce^{BT},$$

provided the temperature dependence appears only in the heating term and not in the viscoelastic memory integral in the Maxwell rheology.

A.2 Spherical Harmonic Functions

In this section of appendix, we give the definition and main properties of spherical harmonic functions, along with the most important formulas related to them that are used in this thesis. Spherical harmonic functions are a set of functions defined on a sphere, meaning they depend on two spherical coordinates: the azimuthal angle θ and the longitudinal angle ϕ. They play an important role in many areas of physics, such as electrodynamics, mechanics, and quantum theory, especially in problems that involve spherical symmetry. This is also why they are commonly used in geophysics and planetary science, where we often deal with objects that are approximately spherical. They are in scalar, vector and tensor form as well. The main reference for the material presented in this section is the book by Varshalovich, Moskalev, and Khersonskii [16], which provides a comprehensive treatment of angular momentum theory and spherical harmonic functions.

A.2.1 Scalar Spherical Harmonic Functions

The complex scalar spherical harmonic functions are defined as

$$Y_{jm}(\theta, \phi) = \begin{cases} N_{jm} P_{jm}(\cos\theta) \exp(im\phi) & m \geq 0, \\ (-1)^m Y^*_{j,-m}(\theta, \phi) & m < 0. \end{cases} \tag{A.3}$$

where $P_{jm}(\cos\theta)$ are the associated Legendre polynomials, and the normalization factor N_{jm} is given by

$$N_{jm} = \sqrt{\frac{(2j+1)}{4\pi} \frac{(j-m)!}{(j+m)!}}. \tag{A.4}$$

A key property of spherical harmonics is that, just like trigonometric functions in one dimension, they form an orthonormal basis for the space of square-integrable functions on a sphere. The orthonormality condition is written as

$$\int_\Omega Y_{j_1 m_1} Y^*_{j_2 m_2} \, d\Omega = \int_0^{2\pi} \int_0^{\pi} Y_{j_1 m_1} Y^*_{j_2 m_2} \sin\theta \, d\theta \, d\phi = \delta_{j_1 j_2} \delta_{m_1 m_2}. \tag{A.5}$$

Since they form a complete basis, this means that for any square-integrable function on the sphere, we can always find a finite expansion that approximates it as closely as desired:

$$\forall \epsilon > 0, \quad \exists j_\epsilon \quad \text{such that} \quad \left\| f(\theta,\phi) - \sum_{j=0}^{j_\epsilon} \sum_{m=-j}^{j} f_{jm} Y_{jm}(\theta,\phi) \right\|_{L_2(\Omega)} < \epsilon. \tag{A.6}$$

This means that any function on a sphere can be approximated by a finite sum of spherical harmonics:

$$f(r,\theta,\phi) = \sum_{j=0}^{j_{\max}} \sum_{m=-j}^{j} f_{jm}(r) Y_{jm}(\theta,\phi). \tag{A.7}$$

The coefficients $f_{jm}(r)$ are obtained using the orthonormality condition:

$$f_{jm} = \int_\Omega f(\theta,\phi) Y^*_{jm}(\theta,\phi)\, d\Omega. \tag{A.8}$$

Another useful property of spherical harmonics is that for negative m, they are related to their positive counterparts by

$$Y_{j,-m} = (-1)^m Y^*_{jm}. \tag{A.9}$$

This means that if a function decomposed into spherical harmonics is real, then the coefficients for negative m can be written as

$$f_{j,-m} = (-1)^m f^*_{jm}. \tag{A.10}$$

This property is useful because it allows us to work only with coefficients for non-negative values of m, which reduces the amount of computations.

During numerical calculations, it's useful to store the harmonic coefficients in a single-index array rather than using two separate indices (j,m). This is done using a so-called multi-index mapping, which is defined for scalar harmonics as:

$$i_s(j,m) = \frac{j(j+1)}{2} + m + 1. \tag{A.11}$$

A.2.2 Vector Spherical Harmonic Functions

This can be extended to vector functions, meaning there exists a similar set of vector spherical harmonic functions with analogous properties, forming a basis for square-integrable vector functions on a sphere. They use a modified Cartesian basis, related to the classical Cartesian basis as

$$\mathbf{e}_1 = \frac{1}{\sqrt{2}}(\mathbf{e}_x + i\mathbf{e}_y), \quad \mathbf{e}_{-1} = \frac{1}{\sqrt{2}}(\mathbf{e}_x - i\mathbf{e}_y), \quad \mathbf{e}_0 = \vec{e}_z. \tag{A.12}$$

These modified basis vectors satisfy the properties

$$\mathbf{e}^*_\mu \cdot \mathbf{e}_\nu = \delta_{\mu\nu}, \quad \mathbf{e}^*_\mu = (-1)^\mu \mathbf{e}_{-\mu}. \tag{A.13}$$

Then the spherical harmonic vectors are defined as

$$\mathbf{Y}^l_{jm}(\theta,\phi) = \sum_{\mu\nu} C^{jm}_{l\nu 1\mu} Y_{l\nu}(\theta,\phi)\mathbf{e}_\mu, \tag{A.14}$$

where $C^{jm}_{l\nu 1\mu}$ are the Clebsch-Gordon coefficients, which will be discussed later in this appendix. The index l represents the component index. The spherical harmonic vector has three components: $j+1$, j, and $j-1$ for a given degree and order j, m. However, for the degenerate case $j = 0, m = 0$, only one vector component is nonzero:

$$\mathbf{Y}^1_{00} = -\frac{\mathbf{e}_r}{\sqrt{4\pi}}. \tag{A.15}$$

The vector component $\mathbf{Y}^j_{jm}$ describes the toroidal part of the vector field, while the components $\mathbf{Y}^{j-1}_{jm}$ and $\mathbf{Y}^{j+1}_{jm}$ describe the spheroidal part.

The spherical harmonic vectors again satisfy the orthogonality condition

$$\int_0^{2\pi}\int_0^{\pi} \mathbf{Y}^{l_1}_{j_1 m_1}(\theta,\phi)\cdot\mathbf{Y}^{l_2 *}_{j_2 m_2}(\theta,\phi)\sin\theta\, d\theta\, d\phi = \delta_{j_1 j_2}\delta_{m_1 m_2}\delta_{l_1 l_2}, \tag{A.16}$$

and they form a basis, so that every square-integrable vector field can be decomposed into a series:

$$\mathbf{f}(r,\theta,\phi) = \sum_{j=0}^{\infty}\sum_{m=-j}^{j}\sum_{l=|j-1|}^{j+1} f^l_{jm}(r)\mathbf{Y}^l_{jm}(\theta,\phi), \tag{A.17}$$

where the coefficients are given by the integral

$$f^l_{jm}(r) = \int_0^{2\pi}\int_0^{\pi} \mathbf{f}(r,\theta,\phi)\cdot\mathbf{Y}^{l*}_{jm}(\theta,\phi)\sin\theta\, d\theta\, d\phi, \tag{A.18}$$

which follows from the orthogonality.

The vector fields for negative orders $-m$ are again related to the positive ones with a slightly more complicated sign rule:

$$\mathbf{Y}^l_{j,-m} = (-1)^{j+m+l+1}\mathbf{Y}^{l*}_{jm}, \tag{A.19}$$

which again leads to a similar rule for the coefficients of a real vector field:

$$f^l_{j,-m} = (-1)^{j+m+l+1} f^{l*}_{jm}. \tag{A.20}$$

While working with the vector spherical harmonics, we again store the harmonic coefficients of a field in a single indexed array using the multi-index

$$i_v(j,m) = 3\left(\frac{j(j+1)}{2} + m\right) + l - j. \tag{A.21}$$

A.2.3 Tensor Spherical Harmonic Functions

The concept of spherical harmonics can be further extended to tensors. The tensorial basis is defined as

$$\mathbf{e}_{k\lambda} = \sum_{\mu\nu} C^{k\lambda}_{\mu 1\nu}\mathbf{e}_\mu\mathbf{e}_\nu, \tag{A.22}$$

where different components correspond to specific tensor parts:

$$\begin{aligned} \mathbf{e}_{00} &\quad \text{(isotropic part)},\\ \mathbf{e}_{1-1}, \mathbf{e}_{10}, \mathbf{e}_{11} &\quad \text{(antisymmetric part)},\\ \mathbf{e}_{2-2}, \mathbf{e}_{2-1}, \mathbf{e}_{20}, \mathbf{e}_{21}, \mathbf{e}_{22} &\quad \text{(traceless symmetric part)}. \end{aligned} \tag{A.23}$$

The spherical harmonic tensors are then defined as

$$\mathbf{Y}^{lk}_{jm}(\theta,\phi) = \sum_{\mu\nu} C^{jm}_{\mu l\nu k} Y_{l\mu}(\theta,\phi)\mathbf{e}_{k\nu}. \tag{A.24}$$

The tensorial coefficients now have four indices, including two component indices. They are divided into the isotropic part ($k = 0$), the antisymmetric part ($k = 1$), and the traceless symmetric part ($k = 2$). In our simulations, we primarily work with traceless symmetric tensors, so we usually keep $k = 2$.

The spherical harmonic tensors satisfy an orthonormality condition similar to the scalar and vector cases:

$$\int_0^{2\pi}\int_0^{\pi} \mathbf{Y}^{l_1k_1}_{j_1m_1}(\theta,\phi)\cdot\mathbf{Y}^{l_2k_2*}_{j_2m_2}(\theta,\phi)\sin\theta\,d\theta\,d\phi = \delta_{j_1j_2}\delta_{m_1m_2}\delta_{l_1l_2}\delta_{k_1k_2}. \tag{A.25}$$

Since they form a complete basis, every square-integrable tensor field can be expanded into a harmonic series:

$$\mathbf{F}(r,\theta,\phi) = \sum_{j=0}^{\infty}\sum_{m=-j}^{j}\sum_{k=0}^{2}\sum_{l=|j-k|}^{j+k} F^{lk}_{jm}(r)\mathbf{Y}^{lk}_{jm}(\theta,\phi). \tag{A.26}$$

The coefficients in this expansion are given by the projection integral:

$$F^{lk}_{jm}(r) = \int_0^{2\pi}\int_0^{\pi} \mathbf{F}(r,\theta,\phi)\cdot Y^{lk*}_{jm}(\theta,\phi)\sin\theta\,d\theta\,d\phi. \tag{A.27}$$

A similar relation holds for spherical harmonics of negative order $-m$, analogous to the vector case:

$$Y^{lk}_{j,-m} = (-1)^{j+m+l+k} Y^{lk*}_{jm}. \tag{A.28}$$

From this, we obtain the corresponding relation for the coefficients of a real tensor field:

$$F^{lk}_{j,-m} = (-1)^{j+m+l+k} F^{lk*}_{jm}. \tag{A.29}$$

The symmetric Cauchy stress tensor can be expressed in terms of these tensor spherical harmonics:

$$\mathbf{t} = \sum_{jm}\left(t^{j0}_{jm}\mathbf{Y}^{j0}_{jm} + t^{j-2,2}_{jm}\mathbf{Y}^{j-2,2}_{jm} + t^{j-1,2}_{jm}\mathbf{Y}^{j-1,2}_{jm} + t^{j2}_{jm}\mathbf{Y}^{j2}_{jm} + t^{j+1,2}_{jm}\mathbf{Y}^{j+1,2}_{jm} + t^{j+2,2}_{jm}\mathbf{Y}^{j+2,2}_{jm}\right), \tag{A.30}$$

where the first term represents the pressure component, while the remaining terms correspond to the deviatoric part, which is important in Maxwell's rheology. The cases $j = 0$ and $j = 1$ represent degenerate states with fewer components.

We again use a multi-index for the components of a deviatoric tensor to store it in a single indexed array,

$$j \le 1 \Rightarrow i_t(j,m) = 3\left(\frac{j(j+1)}{2} + m\right) + l - j - 1, \tag{A.31}$$

$$j > 1 \Rightarrow i_t(j,m) = 5\left(\frac{j(j+1)}{2} + m\right) + l - j - 5. \tag{A.32}$$

A.2.4 Clebsch-Gordan Coefficients

Clebsch-Gordan coefficients $C^{jm}_{j_1 m_1 j_2 m_2}$ originate in quantum mechanics, where they describe the transformation between a coupled angular momentum state labeled by total angular quantum numbers j, m and the uncoupled state labeled by individual quantum numbers j_1, j_2, m_1, m_2. Since quantum mechanical states form an orthonormal basis, these coefficients inherit several useful orthogonality properties and appear frequently when working with spherical harmonics. They are particularly important in the definition of vector and tensor spherical harmonics.

The Clebsch-Gordan coefficients are nonzero only if certain conditions are satisfied. First, the quantum numbers must be non-negative:

$$j \geq 0, \quad j_1 \geq 0, \quad j_2 \geq 0.$$

The magnetic quantum numbers must also be within valid ranges:

$$|m| \leq j, \quad |m_1| \leq j_1, \quad |m_2| \leq j_2.$$

Additionally, the indices must satisfy the triangle inequality:

$$|j_1 - j_2| \leq j \leq j_1 + j_2. \tag{A.33}$$

The total magnetic quantum number is conserved, meaning that:

$$m = m_1 + m_2. \tag{A.34}$$

Moreover, if $m = m_1 = m_2 = 0$, then the sum of the quantum numbers must be even:

$$j + j_1 + j_2 \quad \text{must be even.} \tag{A.35}$$

These coefficients also exhibit several symmetry properties, which follow from their definition:

$$C^{jm}_{j_1 m_1 j_2 m_2} = (-1)^{j+j_1+j_2} C^{j-m}_{j_1 - m_1 j_2 - m_2} = (-1)^{j+j_1+j_2} C^{jm}_{j_2 m_2 j_1 m_1}. \tag{A.36}$$

Another set of relations involves factorial expressions:

$$\begin{aligned} C^{jm}_{j_1 m_1 j_2 m_2} &= (-1)^{j_1+m_1} \frac{\prod_j}{\prod_{j_2}} C^{j_2 - m_2}_{j_1 m_1 j m} = (-1)^{j_1+m_1} \frac{\prod_j}{\prod_{j_2}} C^{j_2 m_2}_{j m j_1 - m_1} \\ &= (-1)^{j_2+m_2} \frac{\prod_j}{\prod_{j_1}} C^{j_1 - m_1}_{j - m j_2 m_2} = (-1)^{j_2+m_2} \frac{\prod_j}{\prod_{j_1}} C^{j_1 m_1}_{j_2 - m_2 j m}. \end{aligned} \tag{A.37}$$

For specific cases, the Clebsch-Gordan coefficients take the following values:

$$C^{j+1,0}_{j010} = \sqrt{\frac{j+1}{2j+1}}, \quad C^{j-1,0}_{j010} = -\sqrt{\frac{j}{2j+1}}. \tag{A.38}$$

For $j_2 = 0$ and $m_2 = 0$, they reduce to Kronecker delta functions:

$$C^{jm}_{j_1 m_1 00} = \delta_{j j_1} \delta_{m m_1}. \tag{A.39}$$

Another special case for $j = 0$ leads to:

$$C^{00}_{j_1 m_1 j_2 m_2} = \frac{(-1)^{j_1+m_1}}{\prod_{j_1}} \delta_{j_1 j_2} \delta_{m_1, -m_2}. \tag{A.40}$$

One of the most important properties of Clebsch-Gordan coefficients is their orthogonality relations:

$$\sum_{m_1 m_2} C^{jm}_{j_1 m_1 j_2 m_2} C^{j'm'}_{j_1 m_1 j_2 m_2} = \delta_{jj'}\delta_{mm'}. \tag{A.41}$$

Another useful orthogonality relation comes from summing over total quantum numbers:

$$\sum_{m m_1} C^{jm}_{j_1 m_1 j_2 m_2} C^{jm_3}_{j_1 m_1 j_3 m_3} = \frac{\prod_j}{\prod_{j_2}} \delta_{j_2 j_3}\delta_{m_2 m_3}. \tag{A.42}$$

A.2.5 Wigner 6j-symbols

Another important set of symbols in spherical harmonic analysis are Wigner's 6j symbols, which appear in formulas describing the action of differential operators on the product of a radially dependent function and a spherical harmonic.

The Wigner 6j-symbol is a number determined by six indices, and it is denoted as:

$$\begin{Bmatrix} j_1 & j_2 & j_3 \\ l_1 & l_2 & l_3 \end{Bmatrix} \tag{A.43}$$

These symbols can be related to Clebsch-Gordan coefficients through the following equation, which can be considered as their definition:

$$\begin{aligned} &\sum_{n_1,n_2,n_3} C^{j_3 m_3}_{l_1 n_1 l_2 n_2} C^{j_1 m_1}_{l_3 n_3 l_2 n_2} C^{l_3 n_3}_{l_1 n_1 j_2 m_2} = \\ &= (-1)^{j_1+l_2+l_3} \Pi_{j_3 l_3} C^{j_1 m_1}_{j_2 m_2 j_3 m_3} \times \begin{Bmatrix} l_1 & l_2 & j_3 \\ j_1 & j_2 & l_3 \end{Bmatrix} \end{aligned} \tag{A.44}$$

They exhibit important symmetry properties, such as invariance under arbitrary permutations of columns:

$$\begin{Bmatrix} j_1 & j_2 & j_3 \\ l_1 & l_2 & l_3 \end{Bmatrix} = \begin{Bmatrix} j_2 & j_3 & j_1 \\ l_2 & l_3 & l_1 \end{Bmatrix} = \begin{Bmatrix} j_3 & j_1 & j_2 \\ l_3 & l_1 & l_2 \end{Bmatrix}, \tag{A.45}$$

as well as invariance under the exchange of upper and lower indices in any two columns:

$$\begin{Bmatrix} j_1 & j_2 & j_3 \\ l_1 & l_2 & l_3 \end{Bmatrix} = \begin{Bmatrix} l_1 & l_2 & j_3 \\ j_1 & j_2 & l_3 \end{Bmatrix} = \begin{Bmatrix} j_1 & l_2 & l_3 \\ l_1 & j_2 & j_3 \end{Bmatrix} \tag{A.46}$$

As a result of these two properties, the symbols also satisfy cross-symmetry:

$$\begin{Bmatrix} j_1 & j_2 & j_3 \\ l_1 & l_2 & l_3 \end{Bmatrix} = \begin{Bmatrix} l_2 & l_1 & j_3 \\ j_2 & j_1 & l_3 \end{Bmatrix} \tag{A.47}$$

And below are some useful evaluations for special choices of the indexes.

$$\begin{Bmatrix} j_1 & j_2 & j \\ l_1 & l_2 & 0 \end{Bmatrix} = \frac{(-1)^{j_1+j_2+j}}{\Pi_{j_1 j_2}} \delta_{j_1 l_2} \delta_{j_2 l_1}, \tag{A.48}$$

$$\begin{Bmatrix} j & 2 & j-2 \\ 1 & j-1 & 1 \end{Bmatrix} = \frac{1}{\sqrt{5(2j-1)}}, \tag{A.49}$$

$$\begin{Bmatrix} j & 2 & j+2 \\ 1 & j+1 & 1 \end{Bmatrix} = \frac{1}{\sqrt{5(2j+3)}}, \tag{A.50}$$

$$\begin{Bmatrix} j & j & 2 \\ 1 & 1 & j-1 \end{Bmatrix} = \sqrt{\frac{(j+1)(2j+3)}{2 \cdot 3 \cdot 5 \cdot j(2j-1)(2j+1)}}, \tag{A.51}$$

$$\begin{Bmatrix} j & j & 2 \\ 1 & 1 & j+1 \end{Bmatrix} = \sqrt{\frac{j(2j-1)}{2 \cdot 3 \cdot 5 \cdot (2j+3)(j+1)(2j+1)}}, \tag{A.52}$$

$$\begin{Bmatrix} j & 1 & j \\ 2 & j+1 & 1 \end{Bmatrix} = -\sqrt{\frac{j+2}{2 \cdot 5 \cdot (j+1)(2j+1)}}, \tag{A.53}$$

$$\begin{Bmatrix} j & 1 & j \\ 2 & j-1 & 1 \end{Bmatrix} = -\sqrt{\frac{j-1}{2 \cdot 5 \cdot j(2j+1)}}, \tag{A.54}$$

$$\begin{Bmatrix} j & j & 1 \\ 1 & 1 & j+1 \end{Bmatrix} = \sqrt{\frac{j}{2 \cdot 3 \cdot (j+1)(2j+1)}}, \tag{A.55}$$

$$\begin{Bmatrix} j & j & 1 \\ 1 & 1 & j-1 \end{Bmatrix} = -\sqrt{\frac{j+1}{2 \cdot 3 \cdot j(2j+1)}}. \tag{A.56}$$

A.2.6 Differential Operators

In this section are the formulas for the action of differential operators on products of radial dependent functions and spherical harmonics. Those our necessary in the spectral method for derivation of the equation for the harmonic coefficients after substituting the harmonic series into the partial differential

equations

$$\Delta\left[f(r)Y_{jm}\right] = \left[\frac{d^2f(r)}{dr^2} + \frac{2}{r}\frac{df(r)}{dr} - \frac{j(j+1)}{r^2}f(r)\right]Y_{jm}, \tag{A.57a}$$

$$\nabla[f(r)Y_{jm}] = \frac{1}{\sqrt{2j+1}}\left[\sqrt{j}\left(\frac{d}{dr} + \frac{j+1}{r}\right)f(r)\vec{Y}^{j-1}_{jm} - \right.$$
$$\left. - \sqrt{j+1}\left(\frac{d}{dr} - \frac{j}{r}\right)f(r)\vec{Y}^{j+1}_{jm}\right], \tag{A.57b}$$

$$\nabla\cdot[f(r)\mathbf{Y}^l_{jm}] = \frac{1}{\sqrt{2j+1}}\left[\sqrt{j}\left(\frac{d}{dr} - \frac{j-1}{r}\right)\delta_{l,j-1} - \right.$$
$$\left. - \sqrt{j+1}\left(\frac{d}{dr} + \frac{j+2}{r}\right)\delta_{l,j+1}\right]f(r)Y_{jm}, \tag{A.57c}$$

$$\nabla[f(r)\mathbf{Y}^l_{jm}] = \tag{A.57d}$$

$$= (-1)^{j+l+1}\sum_k \sqrt{2k+1}\sqrt{l}\begin{Bmatrix}1 & 1 & k\\ j & l-1 & l\end{Bmatrix}\left(\frac{d}{dr} + \frac{l+1}{r}\right)f(r)\mathbf{Y}^{l-1,k}_{jm}$$
$$+(-1)^{j+l}\sum_k \sqrt{2k+1}\sqrt{l+1}\begin{Bmatrix}1 & 1 & k\\ j & l+1 & l\end{Bmatrix}\left(\frac{d}{dr} - \frac{l}{r}\right)f(r)\mathbf{Y}^{l+1,k}_{jm} \tag{A.57e}$$

$$\nabla\times f(r)\mathbf{Y}^l_{jm} = -i\sqrt{6}(-1)^{j+l}\sqrt{l+1}\begin{Bmatrix}l & j & 1\\ 1 & 1 & l+1\end{Bmatrix}\left(\frac{l}{r} - \frac{d}{dr}\right)f(r)\mathbf{Y}^{l+1}_{jm} -$$
$$- i\sqrt{6}(-1)^{j+l}\sqrt{l}\begin{Bmatrix}l & j & 1\\ 1 & 1 & l-1\end{Bmatrix}\left(\frac{l+1}{r} + \frac{d}{dr}\right)f(r)\mathbf{Y}^{l-1}_{jm}, \tag{A.57f}$$

$$\nabla\cdot[f(r)\mathbf{Y}^{lk}_{jm}] = (-1)^{j+l}\sqrt{2k+1}\times\left[\sqrt{l+1}\begin{Bmatrix}1 & l & l+1\\ j & 1 & k\end{Bmatrix}\left(\frac{d}{dr} - \frac{l}{r}\right)f(r)\mathbf{Y}^{l+1}_{jm}\right.$$
$$\left. - \sqrt{l}\begin{Bmatrix}1 & l & l-1\\ j & 1 & k\end{Bmatrix}\left(\frac{d}{dr} + \frac{l+1}{r}\right)f(r)\mathbf{Y}^{l-1}_{jm}\right]. \tag{A.57g}$$

A.2.7 Other Useful Formulas

The product of a scalar spherical harmonic with the radial unit vector can be expressed in terms of vector spherical harmonics

$$\mathbf{e}_r Y_{jm} = \frac{1}{\sqrt{2j+1}}\left(\sqrt{j}\,\delta_{l,j-1} - \sqrt{j+1}\,\delta_{l,j+1}\right)\mathbf{Y}^l_{jm}, \tag{A.58}$$

$$\mathbf{e}_r\cdot\mathbf{Y}^l_{jm} = \frac{1}{\sqrt{2j+1}}\left(\sqrt{j}\,\delta_{l,j-1} - \sqrt{j+1}\,\delta_{l,j+1}\right)Y_{jm}. \tag{A.59}$$

The scalar product of two spherical harmonic vectors is given by

$$\mathbf{Y}^{l_1}_{j_1m_1}\cdot\mathbf{Y}^{l_2}_{j_2m_2} = (-1)^{j_2+l_2}\frac{\prod_{j_1j_2l_1l_2}}{\sqrt{4\pi}}\sum_{jm}\frac{1}{\prod_j}C^{j0}_{l_10\,l_20}\,C^{jm}_{j_1m_1\,j_2m_2}\begin{Bmatrix}j_1 & j_2 & j\\ l_2 & l_1 & 1\end{Bmatrix}Y_{jm} \tag{A.60}$$

and scalar product of a tensor spherical harmonic $\mathbf{Y}^{l_1 k_1}_{j_1 m_1}$ with a vector spherical harmonic $\mathbf{Y}^{l_2}_{j_2 m_2}$ is

$$\mathbf{Y}^{l_1 k_1}_{j_1 m_1} \cdot \mathbf{Y}^{l_2}_{j_2 m_2} = (-1)^{k_1+1} \frac{\prod_{j_1 j_2 l_1 l_2 k_1}}{\sqrt{4\pi}} \sum_{jml} C^{l0}_{l_1 0\, l_2 0}\, C^{jm}_{j_1 m_1\, j_2 m_2} \begin{Bmatrix} j & j_1 & j_2 \\ l & l_1 & l_2 \\ 1 & k_1 & 1 \end{Bmatrix} \mathbf{Y}^{l}_{jm}, \quad \text{(A.61)}$$

where the curly bracket is a Wigner 9-j symbol. For us it is enough to know that the 9-j symbol satisfies the following identity:

$$\begin{Bmatrix} 0 & j & j \\ l & k_1 & k_2 \\ l & k_3 & k_4 \end{Bmatrix} = \frac{(-1)^{j+l+k_2+k_3}}{\prod_{jl}} \begin{Bmatrix} k_4 & k_2 & j \\ k_1 & k_3 & l \end{Bmatrix}. \quad \text{(A.62)}$$

The Cartesian unit vectors can also be expressed as linear combinations of vector spherical harmonics:

$$\mathbf{e}_x = \sqrt{2\pi}\left(-\mathbf{Y}^0_{11} + \mathbf{Y}^0_{1,-1}\right), \quad \text{(A.63)}$$

$$\mathbf{e}_y = i\sqrt{2\pi}\left(\mathbf{Y}^0_{11} + \mathbf{Y}^0_{1,-1}\right), \quad \text{(A.64)}$$

$$\mathbf{e}_z = 2\sqrt{\pi}\,\mathbf{Y}^0_{10}. \quad \text{(A.65)}$$

Bibliography

1. Pappalardo, R. T.; Head, J. W.; Greeley, R.; Sullivan, R. J.; Pilcher, C.; Schubert, G.; Moore, W. B.; Carr, M. H.; Moore, J. M.; Belton, M. J. S.; Goldsby, D. L. Geological evidence for solid-state convection in Europa's ice shell. *Nature*. 1998, vol. 391, no. 6665, pp. 365–368. ISSN 1476-4687. Available from DOI: 10.1038/34862.

2. Ojakangas, G. Thermal state of an ice shell on Europa. *Icarus*. 1989, vol. 81, no. 2, pp. 220–241. ISSN 0019-1035. Available from DOI: 10.1016/0019-1035(89)90052-3.

3. Kivelson, Margaret G.; Khurana, Krishan K.; Russell, Christopher T.; Volwerk, Martin; Walker, Raymond J.; Zimmer, Christophe. Galileo Magnetometer Measurements: A Stronger Case for a Subsurface Ocean at Europa. *Science*. 2000, vol. 289, no. 5483, pp. 1340–1343. ISSN 1095-9203. Available from DOI: 10.1126/science.289.5483.1340.

4. Chyba, Christopher F.; Phillips, Cynthia B. Possible ecosystems and the search for life on Europa. *Proceedings of the National Academy of Sciences*. 2001, vol. 98, no. 3, pp. 801–804. ISSN 1091-6490. Available from DOI: 10.1073/pnas.98.3.801.

5. Turcotte, Donald L.; Schubert, Gerald. *Geodynamics*. Cambridge University Press, 2002. ISBN 9780511807442. Available from DOI: 10.1017/cbo9780511807442.

6. Malvern, Lawrence E. *Introduction to the Mechanics of a Continuous Medium*. Englewood Cliffs, NJ: Prentice-Hall, 1969. ISBN 9780134876030.

7. Goldsby, D. L.; Kohlstedt, D. L. Superplastic deformation of ice: Experimental observations. *Journal of Geophysical Research: Solid Earth*. 2001, vol. 106, no. B6, pp. 11017–11030. ISSN 0148-0227. Available from DOI: 10.1029/2000jb900336.

8. Souček, Ondřej; Běhounková, Marie; Čadek, Ondřej; Hron, Jaroslav; Tobie, Gabriel; Choblet, Gaël. Tidal dissipation in Enceladus' uneven, fractured ice shell. *Icarus*. 2019, vol. 328, pp. 218–231. ISSN 0019-1035. Available from DOI: 10.1016/j.icarus.2019.02.012.

9. Petrenko, V.F.; Whitworth, R.W. *Physics of Ice*. OUP Oxford, 1999. ISBN 978-0-19-158134-2. Available also from: https://books.google.cz/books?id=oC941a8lXWIC.

10. Tobie, G.; Čadek, O.; Sotin, C. Solid tidal friction above a liquid water reservoir as the origin of the south pole hotspot on Enceladus. *Icarus*. 2008, vol. 196, no. 2, pp. 642–652. ISSN 0019-1035. Available from DOI: 10.1016/j.icarus.2008.03.008.

11. Maierová, Petra. *Vliv slapového zahřívání na děje v nitrech ledových měsíců*. Prague, 2006. Available also from: http://hdl.handle.net/20.500.11956/6278. Bachelor's thesis. Univerzita Karlova, Matematicko-fyzikální fakulta. Supervisor: Ondřej Čadek; Referee: Ladislav Hanyk.

12. Pauer, Martin. *Forward and Inverse Modeling of Planetary Gravity and Topography*. Prague, 2013. Ph.D. thesis. Charles University, Faculty of Mathematics and Physics. Supervisor: Ondřej Čadek; Consultant: Doris Breuer.

13. Oldroyd, J. G. On the formulation of rheological equations of state. *Proceedings of the Royal Society of London. Series A. Mathematical and Physical Sciences*. 1950, vol. 200, no. 1063, pp. 523–541. Available from doi: 10.1098/rspa.1950.0035.

14. Ashkenazy, Yosef. The surface temperature of Europa. *Heliyon*. 2019, vol. 5, no. 6, e01908. issn 2405-8440. Available from doi: 10.1016/j.heliyon.2019.e01908.

15. Brink, D.M.; Satchler, G.R. *Angular Momentum*. Clarendon Press, 1993. Oxford science publications. isbn 978-0-19-851759-7. Available also from: https://books.google.cz/books?id=NQvyc4puR8gC.

16. Varshalovich, D A; Moskalev, A N; Khersonskii, V K. *Quantum Theory of Angular Momentum*. WORLD SCIENTIFIC, 1988. isbn 9789814415491. Available from doi: 10.1142/0270.